

Measurement of the Plasma Radius in a Vapor Cell using Schlieren Imaging

Master Thesis in Physics

Anna-Maria Bachmann

December 15, 2016

Department for Theoretical Physics I
Heinrich-Heine-Universität Düsseldorf



Supervision HHU: Prof. Dr. Alexander Pukhov

MPP: Dr. Patric Muggli

Prof. Dr. Allen C. Caldwell

Contents

1	Introduction and Motivation	5
2	Plasma Wakefield Acceleration	7
2.1	Plasma Wakefield Acceleration Theory	7
2.1.1	Wave Breaking Field	7
2.1.2	Linear Wakefield Theory	8
2.2	The AWAKE Project at CERN	10
3	Schlieren Imaging as a Diagnostic Method	15
3.1	Basic Concepts of Schlieren Imaging and Shadowgraphy Technique	15
3.2	Direct Shadowgraphy	17
3.3	Schlieren Imaging and Application to Plasma Radius Measurement	18
3.4	Difference between Shadowgraphy and Schlieren Imaging	21
4	Calculation of Schlieren Images with a Plasma Column as a Transparent Object	22
4.1	Electromagnetic Wave in a Medium	22
4.2	Phase Shift through a Plasma Column	24
4.3	Calculation of the Wave Propagation in the Schlieren Setup	25
4.4	Calculated Schlieren Image Results	26
5	Schlieren Imaging of Density Perturbations in Air	29
5.1	Setup of the Experiment	29
5.2	Results Obtained using Shadowgraphy and Schlieren Imaging	30
6	Schlieren Imaging of an Excited Rubidium Column	32
6.1	The Idea of the Experiment	32
6.2	Setup of the Experiment including Wavelength Determination using Spectroscopy	36
6.2.1	Setup of the experiment at MPP	36
6.2.2	Absorption Spectroscopy	38
6.3	Frequency Dependent Schlieren Imaging Results	41
6.3.1	Schlieren Imaging at a Low Temperature	41
6.3.2	Schlieren Imaging without a Cutoff	42
6.3.3	Schlieren Imaging at High Temperatures	44

6.3.4	Radius Determination of the Excited Channel	45
6.3.5	Study of the Pump Beam close to the Transition Frequency	50
7	Outlook: Plasma Radius Measurement at CERN	52
8	Conclusion	56
	List of Figures	57
	Bibliography	59

1 Introduction and Motivation

The project AWAKE (Advanced Wakefield Experiment) builds the first proton driven plasma wakefield accelerator of the world. The principle is illustrated in Figure 1.1. The basic concept is the following: The CERN SPS proton bunch (blue) propagates through a 10 m long rubidium vapor cell (shaded red). Additionally an ionizing laser pulse (red) co-propagates at half of the length of the bunch and creates a plasma (yellow). Therefore, behind the laser pulse, the proton bunch propagates through plasma, which leads to the generation of a wakefield. The specific position of the ionizing laser increases the effectiveness of acceleration significantly by supporting the self-modulation instability (SMI), which divides the beam into short bunches with the period of the plasma frequency. A witness electron bunch (black) is injected into the wakefield. If it is placed at the right position the electrons will be focused and strongly accelerated by the plasma wave. One of the main goals of the project is to reach plasma wakefield amplitudes on the order of 1 GV/m.

Since the transverse component of the wakefield has a significant value up to a radius of

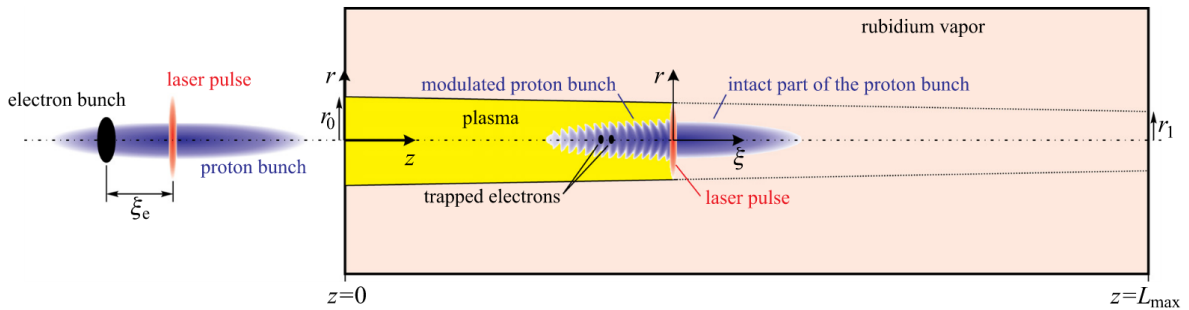


Figure 1.1: Principle of AWAKE [1]

approximately 1 mm the plasma radius must be determined experimentally to ensure its value is larger than along the cell. This measurement is developed in this thesis. Schlieren imaging is an optical method, that allows to increase the contrast of the image of the plasma column. Using Schlieren imaging non-deflected rays of a laser, which act as a background, are blocked, while the transparent object, the plasma column in this case, is imaged by the bent rays. The bending is caused by the change of the index of refraction

and deflection, that is induced by the ionizing laser pulse propagation.

The refractive index of plasma is slightly lower than 1 while the value for vapor is different from 1 for light with a frequency very close to the transition frequency of the given element. Rubidium has a transition line in the visible range from the ground to the first excited state, the D2 line at 780 nm. Using a tunable laser with a wavelength close to the transition wavelength, the effect of the disappearing vapor in the center of the ionizing laser beam becomes visible with Schlieren imaging. The rubidium cell has windows at the ends for the diagnostic and is depicted in Figure 1.2. The ionizing laser (red) propagates along the cell, creates the plasma (yellow) whose transverse profile is visualized by the imaging laser (blue). The imaging laser is a tunable laser and passes through the windows at the end of the cell.

In the present thesis the AWAKE experiment and the need for a plasma radius mea-

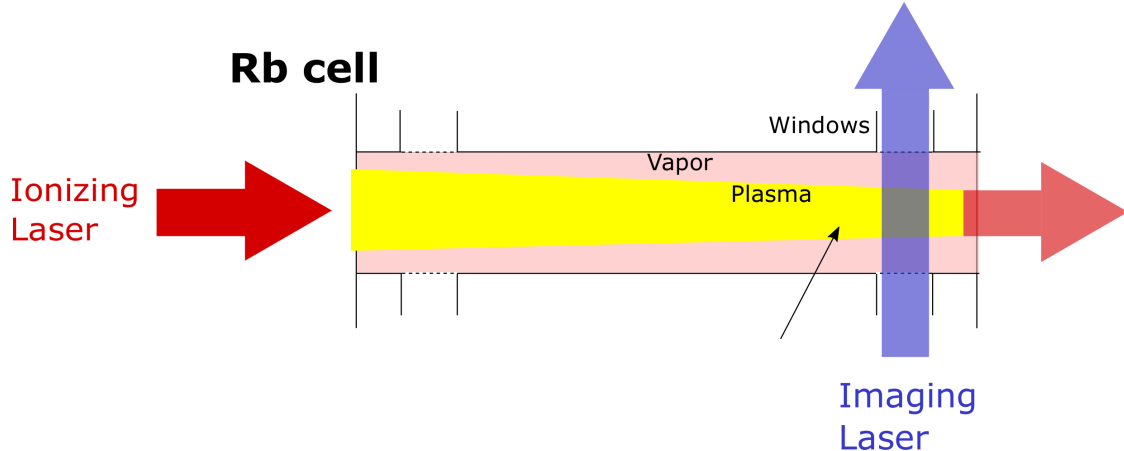


Figure 1.2: Sketch of the 10 m rubidium cell with windows for plasma radius diagnostic (not to scale)

surement are explained in detail. For this purpose, the optical method Schlieren imaging is invented. For a comparison with experimental results, Schlieren images of the plasma column are calculated using Fourier optics. Subsequently, a Schlieren imaging experiment is described, where a gas jet in air is visualized. Finally, Schlieren imaging of a column of excited atoms is described, explaining the experimental setup and presenting experimental results. The developed method should be applied to the plasma radius measurement at CERN, which is outlined in the end.

2 Plasma Wakefield Acceleration

In this chapter the theoretical background, which is necessary to explain the acceleration of charged particles by plasma wakefields, is summarized. First, the basic concept of wakefield acceleration including the formulas to calculate the strength of the fields in linear theory are given. Then, the AWAKE project is described in more detail.

2.1 Plasma Wakefield Acceleration Theory

2.1.1 Wave Breaking Field

The main goal of plasma wakefield acceleration is the acceleration of electrons with a high accelerating gradient of $E = 1 \text{ GeV/m}$ over a distance of $\approx 10 \text{ m}$. A plasma can sustain electron plasma waves with electric fields on the order of the non-relativistic wave breaking field [4]. If a charged particle bunch propagates through the plasma, the plasma particles rearrange to shield the charge. This creates an electrostatic wave. Due to their larger mass ions move much slower than electrons and are neglected in the following. The plasma electron perturbation δn_{pe} depends on the particle bunch density n_b . In linear wakefield theory the perturbation is much smaller than the plasma electron density n_{pe} , i.e. $\delta n_{pe} \ll n_{pe}$. The wave breaking field is defined by the assumption that every plasma electron contributes to the shielding of the particle bunch. With Maxwell's equation and the ansatz for the electric field for a wave propagating in z direction $E = E_0 e^{ikz}$, the wave breaking field E_{Wb} for $\delta n_{pe} = n_{pe}$ is

$$E_{Wb} = m_e c \omega_{pe} / e \quad (2.1)$$

with the plasma frequency ω_{pe} [5]

$$\omega_{pe} = \sqrt{\frac{n_{pe} e^2}{\epsilon_0 m_e}}, \quad (2.2)$$

where ϵ_0 corresponds to the vacuum permittivity, c to the speed of light, m_e to the electron mass and e to the elementary charge. The wave breaking field is an estimate for the upper limit for the electric field in a plasma.

If the particle density of the beam n_b is much smaller than the plasma electron density n_{pe} , i.e. $n_b \ll n_{pe}$, the longitudinal electric field E_z in a plasma is proportional to the wave breaking field:

$$E_z \approx \frac{n_b}{n_{pe}} \cdot E_{Wb}. \quad (2.3)$$

For plasma electron densities from 10^{14} cm^{-3} to 10^{18} cm^{-3} this results in electric fields from approximately 1 GV/m to 100 GV/m for a ratio of $\frac{n_b}{n_{pe}} \approx 1$. Therefore, electron acceleration over a 1 km plasma could already fulfill the requirement of an energy gain of 1 TeV.

2.1.2 Linear Wakefield Theory

Linear wakefield theory is valid for systems with a small plasma density perturbation δn_{pe} , compared to the density of the undisturbed plasma n_{pe} , i.e. $\delta n_{pe} \ll n_{pe}$. At AWAKE this is valid due to the following: $N = 3 \cdot 10^{11}$ particles per bunch of a size of $\sigma_r = 200 \mu\text{m}$ and length of 12 cm leads to the beam density $n_b \approx 1 \cdot 10^{12} \text{ cm}^{-3}$. This is much smaller than the electron plasma density $n_{pe} \approx 1 \cdot 10^{15} \text{ cm}^{-3}$.

To calculate the wakefields, first of all, a variable ζ is introduced, which is moving with the velocity of the driver c :

$$\zeta := ct - z, \quad (2.4)$$

where t is the time and z is the coordinate along the axis.

Using ζ the particle density of the beam can be described easily. Assuming cylindrical symmetry the beam density is separable in two variables:

$$n_b(\zeta, r) = n_{b,\parallel}(\zeta) \cdot n_{b,\perp}(r), \quad (2.5)$$

where r is the radial component, pointing outwards from the axis of propagation of the bunch. Additionally the beam density is assumed to be Gaussian leading to

$$n_{b,\parallel}(\zeta) = n_{b,\parallel,0} \exp\left(-\frac{\zeta^2}{2 \sigma_\zeta^2}\right) \quad (2.6)$$

and

$$n_{b,\perp}(r) = n_{b,\perp,0} \exp\left(-\frac{r^2}{2 \sigma_r^2}\right). \quad (2.7)$$

The respective $\sigma_{r/\zeta}$ are the standard deviation (rms) of the Gaussian function.

The wakefield can be defined in the linear regime using the beam density, see [6]. The longitudinal wakefield $W_z(\zeta, r)$ consists of a longitudinal part $E_{\parallel}(\zeta)$ and a radial part $R(r)$.

More precisely it can be calculated as

$$W_{\parallel}(\zeta, r) = \frac{e}{\epsilon_0} \int_{-\infty}^{\zeta} n_{b,\parallel}(\zeta') \cos(k_p(\zeta - \zeta')) d\zeta' \cdot R(r). \quad (2.8)$$

The transverse wakefield $W_r(\zeta, r)$ can be written as

$$W_{\perp}(\zeta, r) = \frac{e}{\epsilon_0 k_p} \int_{-\infty}^{\zeta} n_{b,\parallel}(\zeta') \sin(k_p(\zeta - \zeta')) d\zeta' \cdot \frac{dR(r)}{dr}. \quad (2.9)$$

The two curves are shifted by $\pi/2$, since the longitudinal field is depending on the cosine of the product $k_p(\zeta - \zeta')$, while the transverse one depends on the sine. The radial component $R(r)$, arising in both equations, can be calculated using the Bessel functions:

$$R(r) = k_p^2 \int_0^r r' dr' n_{b\perp}(r') I_0(k_p r') K_0(k_p r) + k_p^2 \int_r^\infty r' dr' n_{b\perp}(r') I_0(k_p r) K_0(k_p r') \quad (2.10)$$

with I_0 and K_0 representing the zeroth order modified Bessel functions.

For illustration in the following a transverse and longitudinal component of a wakefield created by an relativistic electron bunch is studied. The bunch with a Gaussian density distribution with a size of $\sigma_r = \sigma_\zeta = 0.22$ mm and $N_b = 7 \cdot 10^9$ particles in total is shown at $r = 0$ (black) and at $r = \sigma_r$ (blue). Figure 2.1 shows the longitudinal wakefield (green) depending on the position along the axis ζ at a radius $r = 0$ calculated with Equation 2.8 for a plasma density of $n_{pe} = 1 \cdot 10^{15}$ cm $^{-3}$. In front of the bunch, the wakefield is 0. This is in accordance with the expectation, since the driver is moving with the speed of light, i.e. ahead of the particle bunch can not be a field resulting from the bunch itself. At $\zeta = 0$ plasma electrons are decelerated due to the electron bunch as driver. The transverse wakefield (red) is given at a radius $r = \sigma_r$. It can be observed, that the transverse and longitudinal component of the wakefield is shifted by $\pi/2$. Due to that, 1/4 of the wave is useful for the effective acceleration of charged particles, the part where the wave is focusing and accelerating.

The transverse wakefield at $\zeta = 0$ is plotted in Figure 2.2 in green for the same density and bunch size. The driver particle density is again given in blue. With increasing radial distance to the propagation axis the absolute value of the transverse wakefield increases. It reaches a maximum near the standard deviation ($\sigma_r = \sigma_\zeta = 0.22$ mm) at $r = 0.26$ mm in this case, before it decreases. Since this is at the middle of the electron bunch, plasma electrons are focused. It can be observed that the effect on charges with larger radial distance than $r = 1$ mm can be neglected. The calculation used the parameters used at AWAKE. The spatial extent of the transverse wakefield component leads to the demand

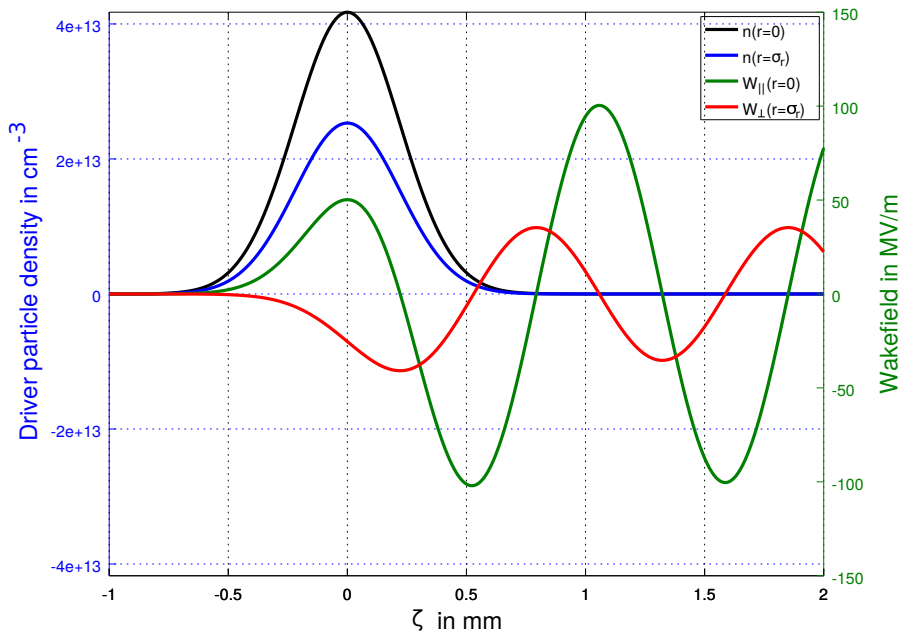


Figure 2.1: Longitudinal wakefield along ζ at $r = \sigma_r$ and transverse wakefield along ζ at $r = 0$ and the driver density distribution at the corresponding radial component

of a plasma radius larger than $r = 1$ mm in the framework of AWAKE.

2.2 The AWAKE Project at CERN

AWAKE develops the first proton driven plasma wakefield accelerator of the world, using the SPS proton bunch at CERN as a plasma wakefield accelerator (PWFA) driver. The main aim of the project is the acceleration of an injected electron bunch. Therefore it covers a broad range of studies such as the self-modulation instability of a proton bunch propagating through a plasma, the generation of long plasmas and short proton bunches and the acceleration of charged particles.

In principle, any charged particle could be used as driver. Proton bunches though carry a larger amount of energy compared to current existing electron or positron bunches. To get an idea about the numbers: It is of interest to reach a witness electron bunch of $N = 2 \cdot 10^{10}$ particles at $E = 500$ GeV, which corresponds to a total energy of $E = 1.6$ kJ. This requires a driver bunch with an energy larger than that. The SPS proton bunch of $N \approx 3 \cdot 10^{11}$ particles at $E = 400$ GeV provides an energy of $E = 19$ kJ and the LHC bunch at $E = 7$ TeV even provides an energy of $E = 336$ kJ, so both would fulfill the condition

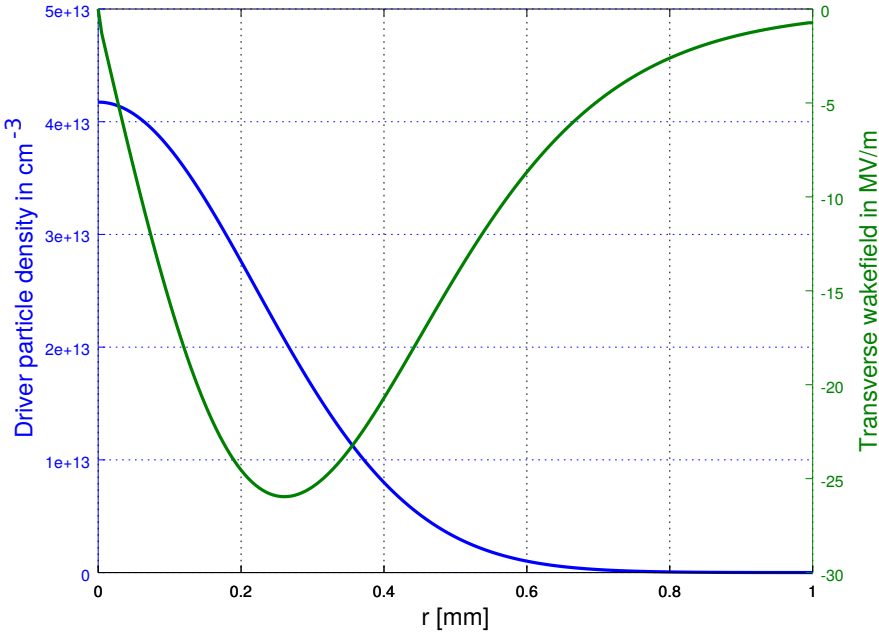


Figure 2.2: Transverse wakefield along r at $\zeta = 0$

[4].

The accelerating gradients of 50 GeV/m could be maintained over m-scales in the plasma, which lead to an energy gain for accelerated electrons up to $E \approx 42 \text{ GeV}$. Simulations adjusted to the LHC p^+ bunch with a proton energy of $E = 1 \text{ TeV}$ and $N_b = 1 \cdot 10^{11}$ protons per bunch result in a gradient larger than 1 GeV/m maintained over hundreds of meters. This means one could accelerate injected electrons up to $E > 500 \text{ GeV}$ in a plasma of the length of $\sim 500 \text{ m}$. Unfortunately, these calculations use a p^+ -bunch of $\sigma_z = 0.1 \text{ mm}$. So far, such short but at the same time high current ($I \approx 20 \text{ kA}$) bunches do not exist.

The length of the driver bunch is an important issue for the plasma wakefield accelerator experiments. A bunch length close to the plasma wavelength leads to an efficient excitation of wakefields, as explained in [8]. It can be understood as the following: The plasma electrons form an ensemble of oscillators, swinging with the plasma frequency ω_{pe} . If the driver contains a Fourier component close to ω_{pe} , the swinging becomes resonant. This condition is fulfilled by a short driver due to the broad spectrum. In subsection 2.1.1 the wave breaking field is defined. An approximation is

$$E_{Wb} \approx \sqrt{\frac{n_{pe} [\text{cm}^{-3}]}{10^{14}}} \text{ GV/m.} \quad (2.11)$$

This means, to reach the desired gradient of GeV/m a plasma electron density of $n_{pe} \approx 10^{14}$ is required. Since the plasma wavelength λ_{pe} is related to the density as

$$\lambda_{pe} \approx \sqrt{\frac{10^{15}}{n_{pe}[\text{cm}^{-3}]}} \text{ mm}, \quad (2.12)$$

the corresponding plasma wavelength is in the order of millimeters. To reach the wave breaking field the driver bunch length should be close to that value. But currently available proton bunches, for example at CERN, have lengths from $\sigma_\zeta = 3 \text{ cm}$ to $\sigma_\zeta = 12 \text{ cm}$. In this context, the AWAKE project benefits from the so called self-modulation instability (SMI). For a long bunch propagating in a dense plasma, i.e. $\sigma_z \gg \lambda_{pe}$, a mechanism, which splits the bunch into smaller bunches, is occurring and utilized at AWAKE. More precisely, under latter condition a bunch train with a period corresponding to the plasma frequency is formed, which leads to a resonant driving of the wakefields to large amplitudes. As mentioned before, the long particle bunch excites a transverse wakefield with periodic focusing and defocusing areas. Due to that a periodic pattern of smaller and higher densities arises. This arrangement reinforces the wakefield amplitude and therefore acts as positive feedback for the growing SMI, see also [4].

In the AWAKE experiment the following parameters are used [4]: The drive bunch, the SPS- p^+ -bunch, has a length of $\sigma_z \approx 120 \text{ mm}$ and $N_b = 3 \cdot 10^{11}$ particles per bunch with an energy of $E = 400 \text{ GeV}$. The beam is focused to $\sigma_r \approx 0.2 \text{ mm}$. It is sent through a cell of the length $L = 10 \text{ m}$, filled with rubidium vapor and a plasma column in the center, that is expected to have a radius of $r \gtrsim 1 \text{ mm}$. Since the plasma is supposed to be fully ionized, the plasma density is equal to the rubidium vapor density, which is $n_{pe} \approx 7 \cdot 10^{14} \text{ cm}^{-3}$. These conditions were chosen to keep the product of the plasma wave number $k_{pe} = \frac{2\pi}{\lambda_{pe}}$ and the radial beam size σ_r smaller than one (i.e. $k_{pe} \cdot \sigma_r \leq 1$) since for $k_{pe} \cdot \sigma_r \gg 1$ the transverse current filamentation instability has to be taken into account [4].

Under the given conditions the SMI would not grow to a measurable level along a 10 m long plasma. Seeding of the instability is necessary. There are different possibilities, for example through a driving wakefield with a preceding laser pulse, a particle bunch with a pulse length of $\sigma_\zeta \leq \frac{2\pi}{w_{pe}}$ or shaping the driver with a sharp rising edge with the same duration. A laser with a moderate intensity of $I < 1 \cdot 10^{13} \frac{\text{W}}{\text{cm}^2}$ creating a relativistic ionization front is the method of choice. The pulse is co-propagating with the p^+ -bunch at its half length and ionizes the rubidium vapor.

Figure 2.3 shows a numerical simulation using a 2D cylindrical geometry. The longitudinal component of the wakefield in units of the wave breaking field $E_{Wb} = 0.96 \text{ GV/m}$ (Equation 2.1 with $n_{pe} = 1 \cdot 10^{14} \text{ cm}^{-3}$) along the p^+ bunch without seeding (black line)

is compared to the results with seeding (red line). The bunch in the simulation is propagating to the right, centered at $\sim 12050 c/\omega_{pe}$ (with $c/\omega_{pe} = 0.53 \text{ mm}$), has a length of $\sigma_z \approx 22.6 c/\omega_{pe}$ (i.e. $\sigma_z \approx 12 \text{ mm}$) and consists of $N_b = 11.5 \cdot 10^{10}$ particles of an energy of $E_b = 450 \text{ GeV}$. The simulation shows the co-propagation of an ionizing laser pulse leads to the seeding of the SMI.

The resulting beam and plasma density structures of the simulations with seeding are

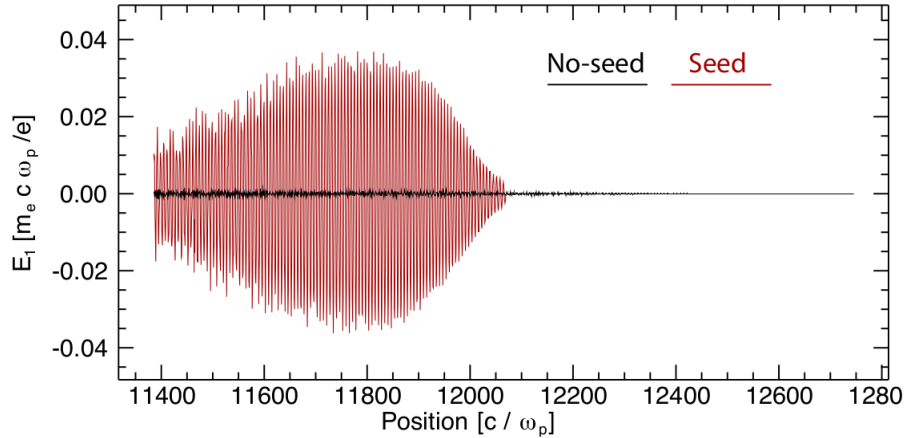


Figure 2.3: Study of the self modulation instability with numerical simulations (OSIRIS code) [4]

visualized in Figure 2.4. A longitudinal section of the self-modulated p^+ beam is depicted. The color indicates the value of the densities depending on the radius r along the longitudinal distance ζ . It shows that the plasma density pattern (colored from white to blue) correlates with the particle bunch density (colored from white to red). The plasma density pattern supports the wakefield, driven by the bunch. The beam radius σ_r and the electron plasma wavelength λ_{pe} are marked in red.

Further in the future a witness electron bunch will be injected into the setup. The electrons will be trapped and accelerated in the wakefield. The plasma radius of $r = 1 \text{ mm}$ is necessary due to the spatial extent of the radial wakefield. Its value needs to be determined experimentally using the optical method Schlieren imaging, which is described in the next chapter.

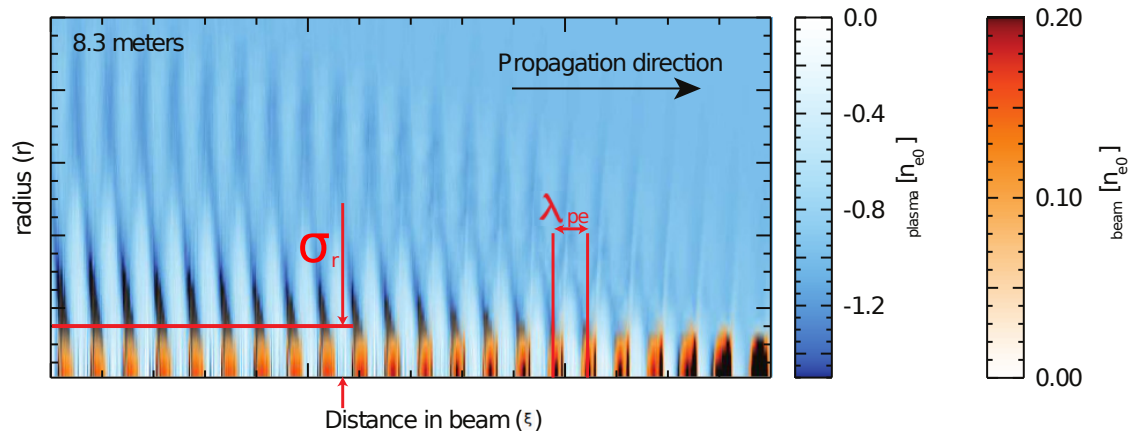


Figure 2.4: Beam and plasma density structure for numerical simulations (OSIRIS code) with seeding of the SMI [4]

3 Schlieren Imaging as a Diagnostic Method

In this chapter the theoretical background of Schlieren imaging, which should be used for the plasma radius measurement, is presented. First, shadowgraphy and Schlieren imaging in general as well as their differences are explained. This then leads to the idea and concept of measuring the plasma radius in the rubidium cell using the difference in the refractive index of vapor and plasma.

3.1 Basic Concepts of Schlieren Imaging and Shadowgraphy Technique

When light propagates through matter its velocity is changed through interaction with the electrons of the material. The index of refraction $n = c/v_\phi$ gives the strength of the interaction, where v_ϕ corresponds to the phase velocity in the medium.

Light in a plasma travels faster than the speed of light. This is shown by the dispersion relation for a transverse electromagnetic wave in a plasma. The light frequency ω is related to the plasma frequency ω_{pe} and the wave number k by [5]

$$\omega^2 = \omega_{pe}^2 + k^2 c^2. \quad (3.1)$$

Therefore, due to the factor of the plasma frequency the phase velocity $v_\phi = \frac{\omega}{k}$ of light in a plasma is always larger than c . This leads to a refractive index of plasma being smaller than that of vacuum ($n = 1$).

It is well known from Snell's law, that rays entering a transition to a medium with different refractive index with an angle are bent. This can be easily explained with the wave nature of light. One can imagine a plane wave propagating through an object with different index of refraction and a curved surface. As mentioned before, light travels either slower or faster through the object, depending on whether the refractive index is higher or lower inside the object than outside. If the object does not consist of two parallel surfaces, the propagation length through the object depends on the transverse component of the waves. Therefore the wave needs more or less time to propagate in space, depending on the transverse position. This transforms the initially plane wave into a wave with a curved

phase plane, the plane where the phase is constant, see Figure 3.1. The wave propagates perpendicular to this plane, which gives the angles of the rays.

These considerations can be applied to the planned plasma radius measurement: The plasma is expected to appear as a column, i.e. cylindrically arranged. Assuming the plasma column is horizontal, a laser beam that is propagating transversely through the column will be bent in vertical directions.

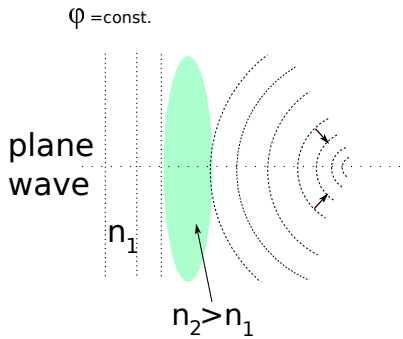


Figure 3.1: Sketch of the phase planes of a wave propagating through an object of higher refractive index with curved surfaces

The index of refraction n is linearly related to the material density ρ through [9]

$$n - 1 = k \cdot \rho, \quad (3.2)$$

where k is the Glad Stone-Dale coefficient. To avoid confusion between density and refractive index, here the gas density is indicated with ρ . This shows that in principle the density could be determined by measuring the index of refraction. Inhomogeneities result in refraction and bending of the light rays.

The ray curvatures for a ray following the optical axis, which concurs with the z-direction of a Cartesian coordinate system can be described mathematically for the bending in x-direction with

$$\frac{\partial^2 x}{\partial z^2} = \frac{1}{n} \frac{\partial n}{\partial x} \quad (3.3)$$

and respectively in y-direction with

$$\frac{\partial^2 y}{\partial z^2} = \frac{1}{n} \frac{\partial n}{\partial y}. \quad (3.4)$$

The deflection angle for a light ray is obtained [9] as

$$\epsilon_x = \frac{1}{n} \int \frac{\partial n}{\partial x} dz \quad (3.5)$$

and

$$\epsilon_y = \frac{1}{n} \int \frac{\partial n}{\partial y} dz. \quad (3.6)$$

Shadowgraphy and Schlieren imaging are both techniques to visualize a transparent object. But as explained in detail in the following sections, their implementation and application differ clearly.

3.2 Direct Shadowgraphy

Direct shadowgraphy describes the simplest possible system, sketched in Figure 3.2. The light of the source propagates through a transparent object towards a screen. Without the object the screen is illuminated uniformly. With the object the changing density (and therefore index of refraction) of the medium bends the light rays. This leads to deficits and concentrations of light at certain areas on the screen.

This technique can be improved by adding a converging lens in front of the object.

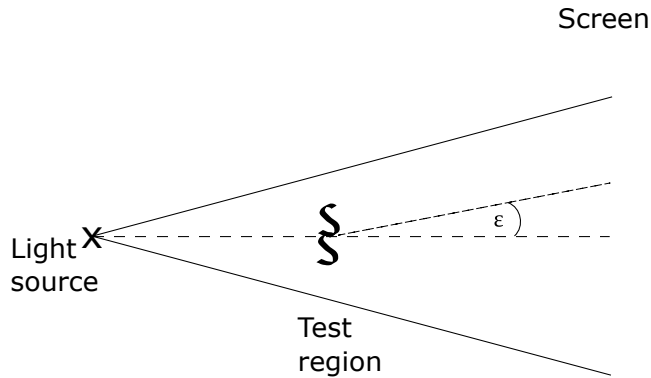


Figure 3.2: Setup of direct shadowgraphy

Figure 3.3 shows the system with a dense spherical object, i.e. with a higher density than the surrounding medium, and a systematic sketch of the image on the screen. Light rays are bent towards regions with higher density. On the surface of the object the lateral gradient is at its maximum which leads to the highest light deflection. Due to that, a bright circle close to the center, resulting from the additionally bent light from the object surface, is visible. It is surrounded by a darker region which comes from the missing rays. Right at the center as well as outside of the object, no deflection takes place. Note that the

size of the object on the screen does not correspond to the real size using shadowgraphy: As explained before, when the planar wavefront is passing the object, the velocity of light inside the object is, in the case of a denser medium, smaller than outside. This leads to a distortion, skewing towards the center. In other words the denser object acts as a lens on the light wave, see also [9]. The size of the object on the screen is therefore depending on the distance between the object and the screen. This is true for small bending angles, or a short distance between the object and the screen. For larger angles or distance, rays could converge in one point and then lead to an inverse image.

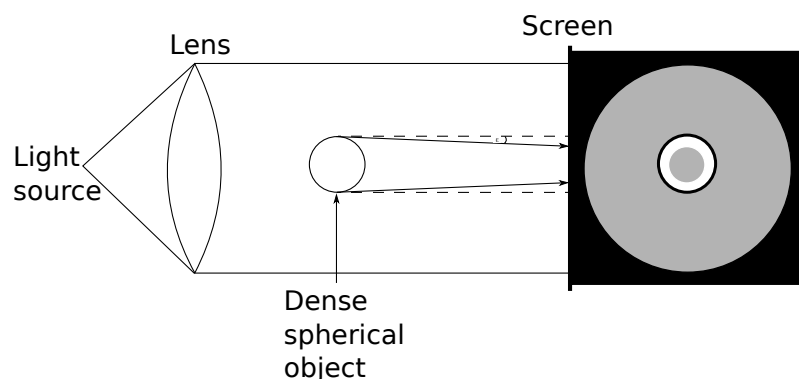


Figure 3.3: Sketch of direct shadowgraphy with a converging lens

3.3 Schlieren Imaging and Application to Plasma Radius Measurement

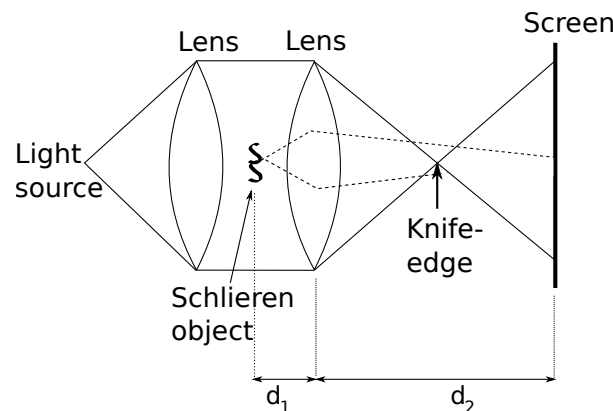


Figure 3.4: Sketch of a simple Schlieren System

For a simple Schlieren imaging system a light source, two lenses and an opaque object are necessary, as pictured in Figure 3.4. The first lens collimates the beam coming from the light source. Since the second lens refocuses the light, an inverted image on the screen with a magnification factor depending on the focal lengths of the two lenses and the distance of the screen is obtained. In other words the whole system acts as a projector. A non-transparent object put in between the lenses would be imaged as silhouette on the screen.

Here imaging condition should be fulfilled, in formula for this case:

$$\frac{1}{d_1} + \frac{1}{d_2} = \frac{1}{f}, \quad (3.7)$$

where d_1 is the distance between the object and the second lens with focal length f and d_2 is the distance between the lens and the screen, see Figure 3.4. If the imaging condition is fulfilled, the position of a ray on a screen is independent of the ray angle at the object. This leads to a sharp image of the object on the screen.

An object which blocks the light is placed in the focal plane of the second lens. This technique is called "cutoff". One possibility is a knife edge, for example a horizontal razor blade, which blocks the light propagating through the lens focus and rays passing either above or below (depending on the orientation of the razor blade). Rays propagating through the Schlieren object are bent and can pass the cutoff if the deflection is away from the knife. Without the cutoff in the focal plane, a fully transparent object with infinite small size could not be imaged with Schlieren imaging, since the imaging condition is fulfilled. Blocking the unbent rays, which act as background illumination, increases the contrast of the transparent object. This enables to image object with a small difference in the index of refraction with Schlieren imaging.

Respecting physical optics, the spot in the focus is not infinite small but has a finite (small) size. The light distribution here corresponds to the Fourier spectrum of the light beam transverse profile [9]. Assuming a Gaussian beam profile in the radial component as before, the light distribution will be Gaussian in the wave number in the focal plane, since the Fourier transformation of a Gaussian function is a Gaussian function. Blocking parts of the light distribution in the focal plane leads to a uniform darkening of the image of the light source on the screen. With a transparent object the bent rays reach the focal plane with a larger distance to the focus of the lens, i.e. appear as peaks at larger wave numbers.

Figure 3.5 presents a sketch how the Schlieren image on the screen results. It shows a central circular object in the y-z-plane and a knife edge as cutoff. For a transparent object with smaller density present, the rays propagating through the upper half of the object

will be bent upwards and can pass the object while the rays through the lower half will be bent downwards and are blocked by the object. This leads to an increase in the intensity of the lower half of the object on the screen and to a decrease in the upper. The image on the screen contains information about the shape and the density of the object. In the plasma radius measurement the gradients can be used to identify the shape of the object in the plasma measurement, since the refractive index of the plasma is uniform.

Another issue at Schlieren imaging is the shape and orientation of the object in the

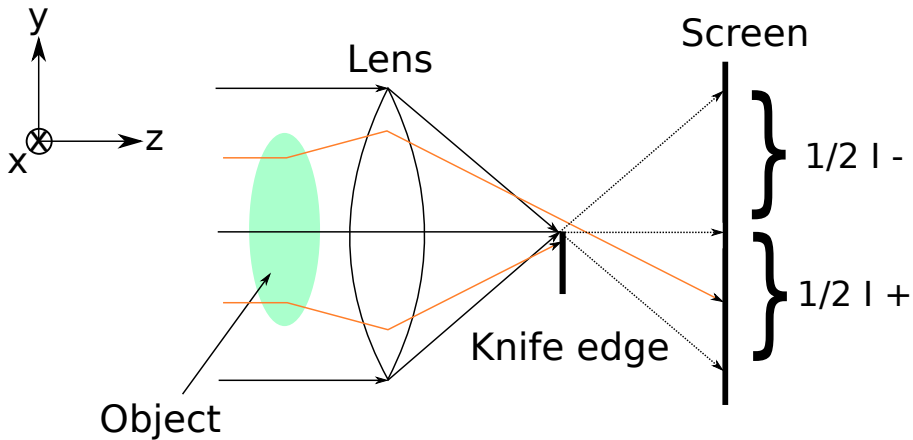


Figure 3.5: The appearance of a cylindrical symmetric object along x with a knife edge orientated along x : Half of the object is brighter, half of it is darker on the screen.

focal plane, since this influences the appearance of the Schlieren object on the screen. A Cartesian coordinate system is defined as the following: the z-axis corresponds to the optical axis of the system, the x-axis points into the plane, while the y-axis goes upwards. A razor blade orientated along x for example shows gradients of the refractive index of the transparent object along y , i.e. $\frac{\partial n}{\partial y}$. This corresponds to the refraction with components perpendicular to the edge. In contrast, rays with a parallel deflection are not blocked by the razor blade. But this also means that a transparent object, which consists only of gradients along x remains invisible. In other words, to achieve the full image of a transparent object with a knife edge as cutoff, in general two images are required, one with an edge orientated along x , one along y . An other opportunity is to use for instance a pinhole instead of the knife edge. This method images gradients along x and y . An overview of the three mentioned objects, used to interfere at the Fourier plane can be found in Figure 3.6. The resulting images of a gas jet for the different cutoffs are shown.

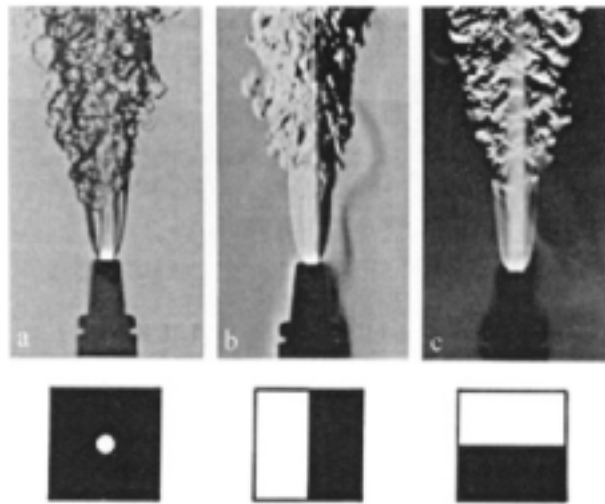


Figure 3.6: Schlieren image of a gas jet using three different cutoffs: a pinhole (a), a knife edge orientated along y (b) and (c) orientated orientated along x [9]

3.4 Difference between Shadowgraphy and Schlieren Imaging

There are main differences between the techniques shadowgraphy and Schlieren imaging. Firstly, while an unfocused image is used with shadowgraphy, the image is formed by a lens with Schlieren imaging. Secondly, in contrast to Schlieren imaging, shadowgraphy does not use an object interacting in the light distribution (cutoff technique). Thirdly, Schlieren imaging displays the deflection angle ϵ of the light ray. The signal of the transparent object is proportional to the first derivative of the refractive index $\frac{\partial n}{\partial x}$ or $\frac{\partial n}{\partial y}$. Shadowgraphy in contrast displays the ray displacement resulting from the deflection, which corresponds to the gradient of the deflection angle. Therefore the signal with shadowgraphy is proportional to the second derivative of the index of refraction $\frac{\partial^2 n}{\partial x^2}$ or $\frac{\partial^2 n}{\partial y^2}$ [9].

In the present thesis Schlieren imaging is developed as a method to visualize the plasma column inside the rubidium vapor cell for the radius determination. The refractive indices of plasma and vapor are different and lead to a bending of the rays propagating through the transparent object, the plasma column in this case.

4 Calculation of Schlieren Images with a Plasma Column as a Transparent Object

Schlieren images of a plasma column are calculated in the following chapter to predict and also to compare with the experimentally results at AWAKE. With the help of Fourier optics the propagation of the electromagnetic wave and the phase shift caused by a transparent object with different refractive index is computed.

4.1 Electromagnetic Wave in a Medium

When an electromagnetic wave propagates through a medium with refractive index n two main processes take place: Absorption, that changes the wave's amplitude and dispersion, that changes the wave phase velocity according to $v_\phi = c/n$. In general, the complex index of refraction n is a function of the light frequency ω , i.e. $n = n(\omega)$.

The refractive index can be divided in a real n' and imaginary part n''

$$n = n' + i n''. \quad (4.1)$$

For an electromagnetic wave

$$E = E_0 e^{i(\omega t - k z)} \quad (4.2)$$

with the wave number

$$k = \frac{2\pi}{\lambda} = n k_0 \quad (4.3)$$

with k_0 corresponding to the wave number in vacuum, it follows for the electromagnetic wave in a medium

$$E = E_0 e^{-k_0 n'' z} e^{i(\omega t - n' k_0 z)} = E_0 \cdot \underbrace{e^{-2\pi n'' z/\lambda}}_{\text{Absorption dep. on } n''} \cdot \underbrace{e^{i k_0 (c_0 t - n' z)}}_{\text{Dispersion dep. on } n'} \quad (4.4)$$

This shows that the imaginary part n'' of the refractive index n of a medium determines the absorption of the electromagnetic wave in the medium, while the dispersion is only dependent on the real part n' . Absorption is used in the present thesis in absorption

spectroscopy for the laser wavelength determination. Dispersion is the phase shift of the wave propagating through an object in Schlieren imaging.

The real and imaginary parts of the refractive index can be derived using a classical model, describing the electrons in the medium as damped harmonic oscillators, excited by the electromagnetic wave [10] as:

$$m_e \ddot{x} + m_e \gamma \dot{x} + m_e \omega_0^2 x = e E_0 e^{i\omega t}. \quad (4.5)$$

Here m_e corresponds to the mass, the damping factor γ corresponds to the excited state decay rate $\gamma = 1/\tau$ with τ the lifetime of the upper atomic state, the transition frequency ω_0 and the electric field of the electromagnetic wave $E = E_0 e^{i\omega t}$ with frequency ω . With the ansatz

$$x = x_0 e^{i\omega t} \quad (4.6)$$

one can determine the amplitude of the oscillation

$$x_0 = \frac{e E_0}{m_e (\omega_0^2 - \omega^2 + i \gamma \omega)}. \quad (4.7)$$

This leads to the induced dipole moment p_{el}

$$p_{el} = e x = \frac{e^2 E_0 e^{i\omega t}}{m_e (\omega_0^2 - \omega^2 + i \gamma \omega)} \quad (4.8)$$

Since the macroscopic polarization for N electrons is $P = N p_{el}$ but also $P = \epsilon_0 (\epsilon - 1) E$ with ϵ the relative permittivity and $n = \sqrt{\epsilon}$ it follows

$$n = \sqrt{1 + \frac{N e^2}{\epsilon_0 m_e (\omega_0^2 - \omega^2 + i \gamma \omega)}}. \quad (4.9)$$

for an atom with one transition stage. More general, in the case of multiple upper states, the following holds

$$n = \sqrt{1 + \frac{N_i e^2}{\epsilon_0 m_e} \sum_{j \neq i} \frac{f_{ij}}{\omega_{ij}^2 - \omega^2 + i \gamma_{ij} \omega}}. \quad (4.10)$$

with N_i standing for the number of electrons in the lower state i , f_{ij} the oscillator strength of a transition, ω_{ij} the transition frequency from state i to j and $\gamma_{ij} = 1/\tau_{ij}$ with τ_{ij} the lifetime of the upper state j . Rubidium has only one valence electrons, i.e. the number of electrons in the lower state corresponds to the number of atoms. In the following, the equation for the refractive index is used to calculate results of Schlieren imaging.

4.2 Phase Shift through a Plasma Column

Phase Shift through an Arbitrary Object

As in section 4.1 derived, the phase shift through an object with a different refractive index influences the electromagnetic wave $E(\vec{r})$ as follows:

$$E_1(\vec{r}) = E_0(\vec{r}) e^{(i \cdot \Delta\phi)}. \quad (4.11)$$

The phase shift of a transparent object is

$$\Delta\phi = k_0 \cdot \Delta n' \cdot d_{object}. \quad (4.12)$$

$\Delta n'$ corresponds to the difference of the real parts of the refractive index between the object and the surrounding medium, in our case between plasma and vapor and d_{object} corresponds to the thickness of the object depending on the coordinates x and y .

Using the parameters determined within the framework of AWAKE in the calculations it will be validated whether a signal for Schlieren imaging can be expected.

Expected Parameters in AWAKE

Since rubidium has only one valence electron, by assuming full ionization due to the high intensity of the ionizing laser, the plasma density n_{pe} will be equal to the vapor density n_0 . Further values used for the calculation can be found in Table 4.1. The refractive index

Electron plasma density n_{pe}	10^{15} cm^{-3}
Transition wavelength λ_{D2}	780.24 nm
Transition frequency ω_{D2}	2.42 PHz
Laser frequency ω_L	$\omega_{D2} + \Delta\omega_L$
Laser detuning frequency $\Delta\omega_L$	$2\pi \cdot (-5) \text{ GHz}$

Table 4.1: Parameters used in the calculations

of vapor can be calculated according to Equation 4.10. Using the values from Table 4.1 the refractive index of vapor in the ground state is

$$n'_{vapor}(N_i = n_0) - 1 \approx 3.66 \cdot 10^{-3}. \quad (4.13)$$

The dispersion relation of an electromagnetic wave with the frequency ω in a plasma is [5]

$$\omega^2 = \omega_{pe}^2 + k^2 c_0^2. \quad (4.14)$$

With $\omega^2 = c^2 k^2$ and $n = c_0/c$ this leads to the refractive index of plasma

$$n_{plasma} = \sqrt{1 - \frac{\omega_{pe}^2}{\omega^2}}, \quad (4.15)$$

which is for the given parameter

$$n_{plasma} - 1 \approx -2.83 \cdot 10^{-7}. \quad (4.16)$$

This leads to a difference of

$$\Delta n' \approx 3.66 \cdot 10^{-3}. \quad (4.17)$$

Together with the radius of the column this defines the phase shift of the electromagnetic wave caused by the plasma.

4.3 Calculation of the Wave Propagation in the Schlieren Setup

In the following Fourier optics are used to calculate the Schlieren images. The particular

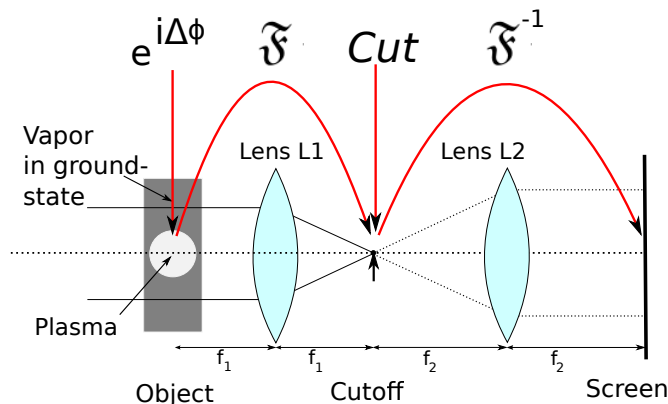


Figure 4.1: Sketch of the setup and the corresponding functions applied in the calculations

system to be calculated consists of a transparent object in the object plane, a thick lens represented by two lenses and a screen in the image plane, see Figure 4.1. The intensity distribution in the object, the focal and the imaging plane can be calculated in a very convenient way.

The light distribution in one focal plane of a lens corresponds to the Fourier transformation of that spectrum in the second focal plane [9]. In particular, the spatial light distribution at the razor blade complies with the light distribution in the frequency domain in the object plane. Similarly, the spatial light distribution on the screen is given by the inverse Fourier

transformation of the spectrum in the cutoff plane. Consequently instead of calculating the amplitude and phase of the electromagnetic wave along the whole system, the following operations were done to receive the intensity distribution in the image plane: The phase shift of the electromagnetic wave caused by the object is applied (Equation 4.18), a Fourier transformation (Equation 4.19) is used, the spatial amplitude spectrum is cut (representing the effect of the razor blade, Equation 4.20) and an inverse Fourier transformation is applied (Equation 4.21). This is written using equation as follows:

$$E_1(\vec{r}) = E_0(\vec{r}) e^{i \Delta \Phi} \quad (4.18)$$

$$E_2(\vec{r}) = \mathfrak{F}\{E_1(\vec{r})\} \quad (4.19)$$

$$E_3(\vec{r}) = \text{Cut}\{E_2(\vec{r})\} \quad (4.20)$$

$$E_4(\vec{r}) = \mathfrak{F}^{-1}\{E_3(\vec{r})\} \quad (4.21)$$

The phase shift caused by the object is calculated in section 4.2. The Fourier transformation is given by

$$\mathfrak{F}\{E(\vec{r})\} = \int_{-\infty}^{\infty} \int_{-\infty}^{\infty} E(\vec{r}) e^{2\pi i (\vec{k} \cdot \vec{r})} d\vec{k} \quad (4.22)$$

and the inverse Fourier transformation by

$$\mathfrak{F}^{-1}\{E'(\vec{k})\} = \int_{-\infty}^{\infty} \int_{-\infty}^{\infty} E'(\vec{k}) e^{2\pi i (\vec{k} \cdot \vec{r})} d\vec{r}. \quad (4.23)$$

The effect of the knife edge was implemented by setting the amplitude of the wave in the cutoff plane to zero for the coordinates of the knife edge. In the following results this is

$$E(\vec{r}) = E(x, y) \equiv 0 \text{ for } y \leq 0. \quad (4.24)$$

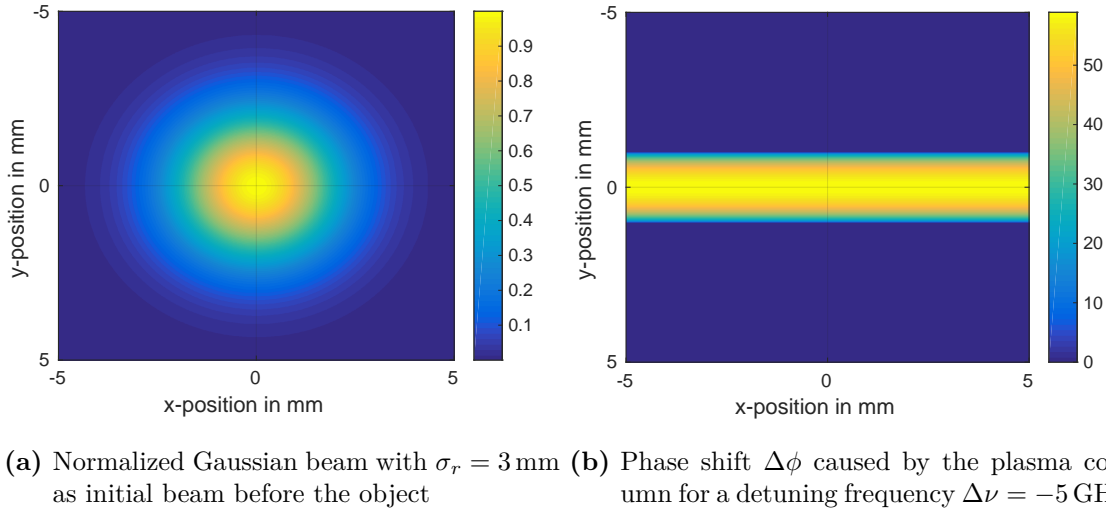
The results of the calculations are given in the next section. The addressed setup and the corresponding functions applied to the electromagnetic wave in the calculations are shown in Figure 4.1.

4.4 Calculated Schlieren Image Results

For simplicity the two lenses of the Schlieren setup have the same focal length ($f_1 = f_2$), i.e. no magnification of the image needs to be considered. Excited vapor is neglected in the following, i.e. only (fully ionized) plasma surrounded by vapor in the ground state is considered.

An initial normalized Gaussian beam with a radius of $\sigma_r = 3 \text{ mm}$ and a plasma column

with a radius $r_{plasma} = 1$ mm is used. The initial beam and the phase shift $\Delta\phi$ over x and y is illustrated in Figure 4.2. In the following the images on the screen are presented,



(a) Normalized Gaussian beam with $\sigma_r = 3$ mm (b) Phase shift $\Delta\phi$ caused by the plasma column for a detuning frequency $\Delta\nu = -5$ GHz

Figure 4.2: Calculated intensity profile of the initial beam and the phase shift caused by the object

depending on the presence of a knife edge in the cutoff plane and of the plasma column as an object.

Without an object but a horizontal knife edge as cutoff in the center i.e. at a position $y = 0$, the Gaussian light distribution remains on the screen but with approximately half of the intensity, see Figure 4.3a.

With the plasma column as an object but without a cutoff the object is not visible on the screen, see Figure 4.3b. Absorption by the plasma is neglected, i.e. only a phase shift is applied to the electromagnetic wave. Without a cutoff the image on the screen is independent of the phase of the wave in the object plane. This observation confirms the principle of the imaging condition.

With the plasma as an object and with a horizontal knife edge as cutoff at a position $y = 0$ the plasma column is visible on the screen. Also its radius of $r = 1$ mm is recognizable. Intensities on the screen reach more than twice the initial peak intensity. This indicates that Schlieren imaging should be suitable for the radius determination in the experiment in the framework of AWAKE. Eventually, the experimental results can be compared with the calculated images.

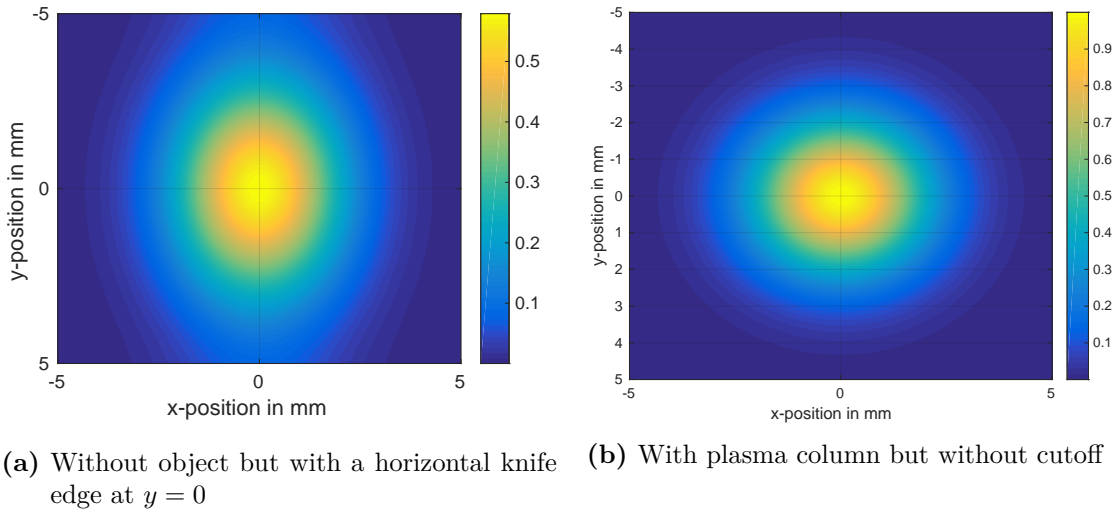


Figure 4.3: Calculated intensity profiles on the screen in the absence of either an object or a cutoff

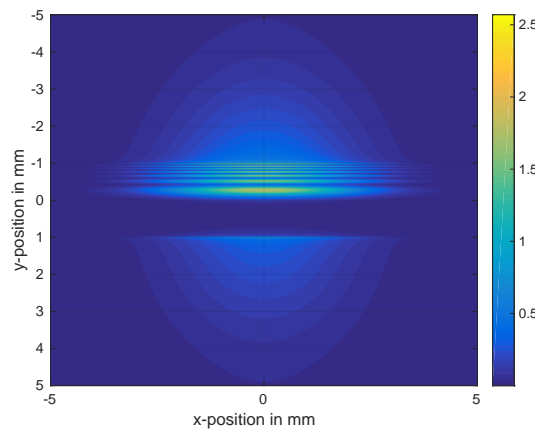


Figure 4.4: With plasma column and a horizontal knife edge as cutoff at $y = 0$

5 Schlieren Imaging of Density Perturbations in Air

In the following chapter the experimental results of Schlieren imaging of density perturbations in air are presented. In this case the difference in index of refraction is large. This serves as a preparation for the experiment in which the transparent object is a column of excited or ionized atoms.

5.1 Setup of the Experiment

The purpose of the setup is to visualize density perturbations in air. They are produced using a compressed air can. Dense air flows out of the can through a nozzle. The gas jet is visualized using Schlieren imaging.

The setup built up at the Max-Planck Institute for Physics (MPP) in Munich is shown in Figure 5.1. A helium-neon laser (HeNe laser) from THORLABS is used as a light source.

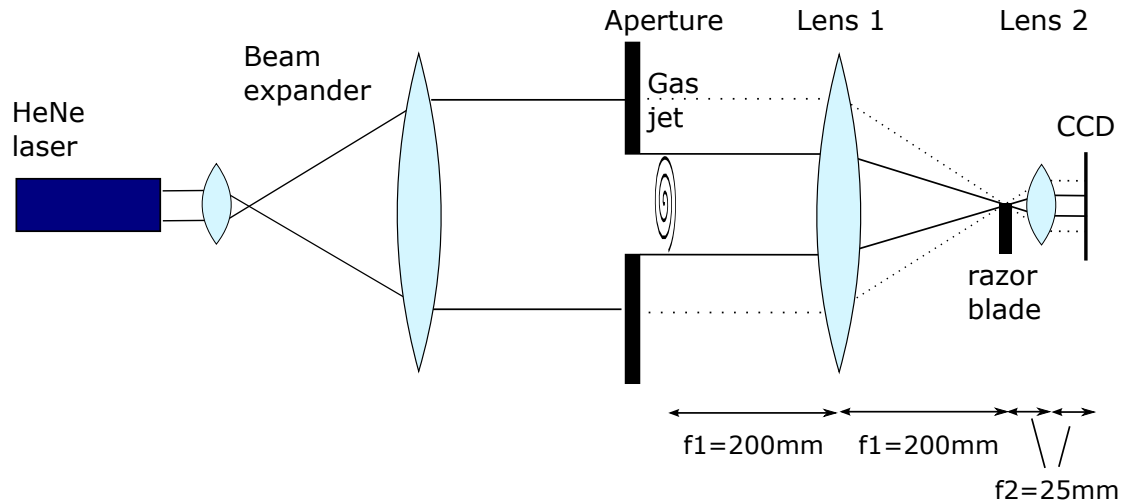


Figure 5.1: Sketch of the setup for schlieren imaging of a gas jet

Its properties are listed in Table 5.1. Images are recorded with the CCD camera "Manta MG-031B" from STEMMER IMAGING, see Table 5.2.

Beam diameter	$0.48 \text{ mm} \pm 3\%$
Wavelength	632.8 nm
Power	0.5 mW

Table 5.1: Data of red HeNe laser from THORLABS

Going from left to right, the HeNe laser beam size is increased with a beam expander to

Resolution	656 x 492
Frame rate	125 fps
Sensor	1/4" CCD
Cell size	5.6 μm
Minimal integration time	58 μs

Table 5.2: Data of the CCD Camera "Manta MG-031B "

visualize large objects. To avoid aberrations caused by the short focal length lens of the telescope, an aperture is placed before the object. Then the light propagates through the "Schlieren setup", consisting of the two lenses and the block, a razor blade in the focal plane, towards the CCD. The camera images the gas jet.

5.2 Results Obtained using Shadowgraphy and Schlieren Imaging

Images of the gas jet are presented in Figure 5.2. The image on the left is produced without using a block. The difference in the air density leads to a difference in the refractive indices, which then leads to the light bending effects. In theory without a block, the transparent object is not expected to be visible at all, since the imaging condition is fulfilled. Consequently, the intensity profile in the image plane should not depend on the angle of the rays in the object plane. Nevertheless, an image of the object appears also without a block. Several reasons could serve as an explanation: Firstly, if rays were bent strongly, it is possible that they are not captured by "Lens 1" as depicted in Figure 5.1. This leads to a lack of intensity in some areas. Secondly, the gas jet has a finite size, which means that not the whole object fulfills imaging condition. This might serve as an explanation for the increased intensities in some areas of the image on the screen. Nonetheless the structure of the gas jet is not clearly visible.

On the right side in Figure 5.2 is depicted the image recorded with a razor blade in the

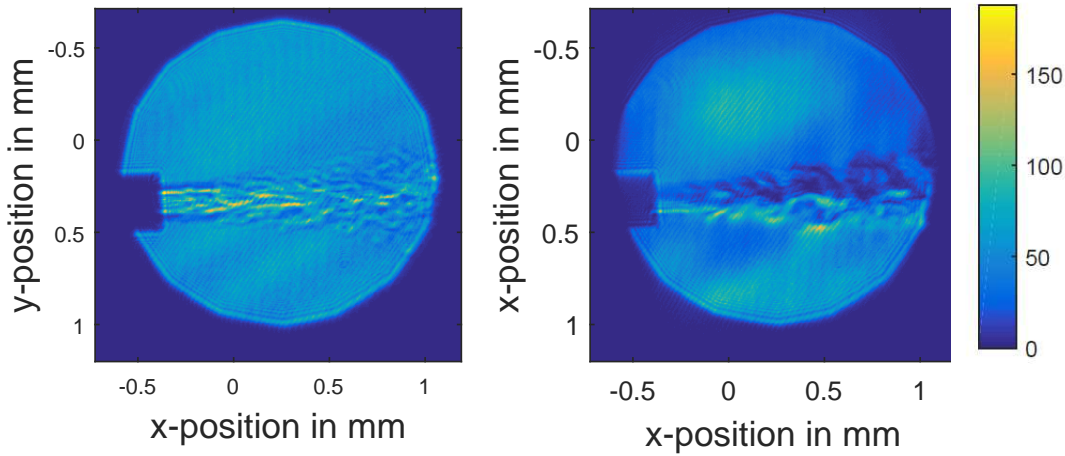


Figure 5.2: Schlieren image of the gas jet without (left) and with (right) cutoff

focus of "Lens 1". Non-bent rays and the bent rays which were passing the focal plane in the lower half are blocked. In this case the structure of the gas jet appears clearly. Note that Schlieren imaging is sensitive to the change in the refractive index, i.e. its gradient. In this experiment the size of the object is visible with and without a block. This is probably due to the large change in index of refraction of the strong air jet. If the difference in the refractive indices between the object and the surrounding medium is smaller, a measurement without the cutoff would not show the object. In this case the non-bent rays constituting the background, need to be blocked to make the object visible. This can be realized with Schlieren imaging and is used for visualizing a column of excited atoms in the following.

6 Schlieren Imaging of an Excited Rubidium Column

In the framework of AWAKE the plasma radius determination will be performed using Schlieren imaging. The experiment in the following chapter applies the method to visualize a column of excited atoms. The approach, the setup and the implementation are explained and the experimental results are discussed.

6.1 The Idea of the Experiment

When an ionizing laser pulse propagates through a rubidium vapor cell as in the AWAKE project, three different zones can be observed: Vapor in the ground state at a larger radius (\approx zero laser intensity), plasma in the center (laser intensity exceeding the ionization intensity) and a transition section of excited, but not ionized atoms. An excited vapor can be created either by the ionizing laser pulse, when its frequency bandwidth overlaps with the rubidium (Rb) D2 optical transition (as in AWAKE), or by the laser beam used for the Schlieren diagnostic as in the experiments here after. This results in regions of different refractive indices.

Equation 4.15, providing the refractive index of plasma, demonstrates that the value is always slightly below one and is only weakly dependent on the laser frequency.

Equation 4.10 shows that the index of refraction is a function of the ground state population of the rubidium atoms, i.e. of the excitation laser beam frequency and intensity. Firstly, the refractive index of vapor is a function of the radius. The numbers of atoms in the lower state N_i depend on the ionizing laser intensity ($I(r)$), which is a function of the radius. Hence also the refractive index of vapor is ($n_{vapor}(N_i(I(r)))$). Secondly, the refractive index increases (or decreases) for laser frequencies close to the transition frequency. Due to that, close to the transition line the difference between the refractive indices of vapor and air or vacuum is much larger than the difference between the refractive indices of plasma and air or vacuum, i.e. $|n'_{vapor} - 1| \gg |n'_{plasma} - 1|$.

Here we use a commercial available laser to probe (and excite) the Rb vapor index of refraction of the vapor near its D2 optical transition. The interaction of the laser beam

with the Rb is strong since the lower state of the transition is the atom ground state (i.e. $N_i = n_{vapor}$) and the index of refraction can be made large by tuning the laser frequency (see Equation 4.10).

This in turn leads to a large difference between the indices of refraction of the plasma and the vapor. We use the tunable laser both as the exciting (ionizing in AWAKE) laser and the Schlieren probing laser. Due to the narrow linewidth of the laser (see Table 6.2) rubidium can be considered as a two-level system with the ground and the first excited state. The refractive index of vapor depending on the detuning frequency $\Delta\nu$ around the transition frequency corresponding to the D2 transition line with a wavelength $\lambda = 780.24\text{ nm}$ is plotted in Figure 6.1 from Equation 4.10. In the calculation the density of the atoms in the ground state N_i corresponds to the vapor density set in the framework of AWAKE ($n = 1 \cdot 10^{15}\text{ cm}^{-3}$). Thus, the graph represents the refractive index of the non-excited rubidium vapor.

The signal of the transparent object using Schlieren imaging increases with increasing

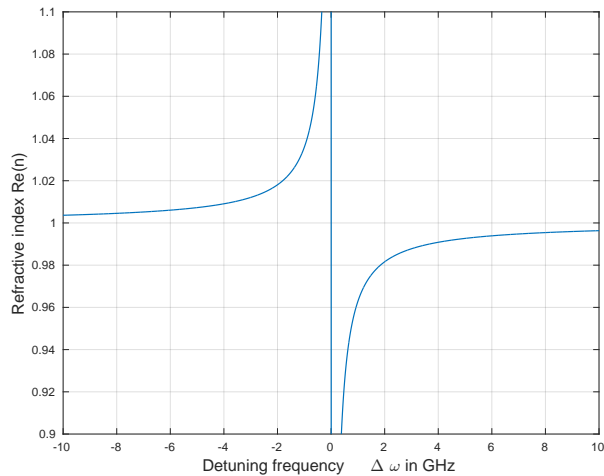


Figure 6.1: Refractive index of the rubidium vapor near the D2 transition line

difference in the refractive indices between the object and the surrounding medium. Consequently, the signal can be enhanced by tuning the laser to operate close to the transition frequency, due to the increasing difference between the refractive indices of the vapor and the plasma in AWAKE and between the excited and non-excited regions of the vapor here. This knowledge lead to the concept of the Schlieren imaging measurement method of the present thesis: The refractive index of vacuum is 1. For an arbitrary laser wavelength the refractive index of the vapor to be ionized is very close to 1. As stated in Equation 4.15 the refractive index of a plasma is always smaller than one. The difficulty within the framework of AWAKE is the small plasma density, leading to a small value of ω_{pe} in

Equation 4.15 and consequently a value very close to 1. To visualize the corresponding weak phase shift of the light propagating through the plasma column is very challenging. However this issue can be dealt with by making use of the strong dependency of the refractive index of the rubidium vapor on laser wavelength if it is close to the transition line (D2 here). Thus, while the difference of the refractive indices between the vacuum and the plasma is small, the difference in index between the vapor and the vacuum or the plasma can be made large. This consideration is depicted in Figure 6.2. For clarity the reality is simplified assuming either non-excited or fully excited vapor without continuous transitions. The graph below the figure shows the refractive index inside the rubidium cell as a function of the radius. The origin is the center of the cell, which is supposed to coincide with the center of the plasma column. The refractive indices are calculated for the densities used in AWAKE ($n \approx 10^{15} \text{ cm}^{-3}$) and a laser detuning frequency of $\Delta\nu = -5 \text{ GHz}$ from the transition line D2. The refractive index values are summarized in Table 6.1. Fully excited vapor represents the case of half of the atoms being in the excited, half of them in the ground state, the maximum obtainable in a two-level atomic system. The values in the table demonstrate that by adjusting the laser frequency, the

Non-excited vapor	$n - 1 \approx 4 \cdot 10^{-3}$
Fully excited vapor	$n - 1 \approx 2 \cdot 10^{-3}$
Plasma	$n - 1 \approx 3 \cdot 10^{-7}$

Table 6.1: Refractive indices for a vapor and plasma density of $n \approx 10^{15} \text{ cm}^{-3}$ and a laser detuning frequency of $\Delta\nu = -5 \text{ GHz}$ from the transition line D2

difference of the refractive indices between the object and the surrounding medium could be increased by more than 4 orders of magnitude.

Another conclusion to be drawn from these considerations is that due to the equal value of the differences of the refractive indices the principle is similar of visualizing a column of excited atoms inside of vapor in the ground state as of visualizing a column of ionized atoms inside of fully excited vapor. This consideration gave rise to the following measurement which uses Schlieren imaging to visualize a column of excited atoms inside of a rubidium vapor cell (i.e. without ionization). The experiment serves as a preparation for the plasma radius measurement at CERN.

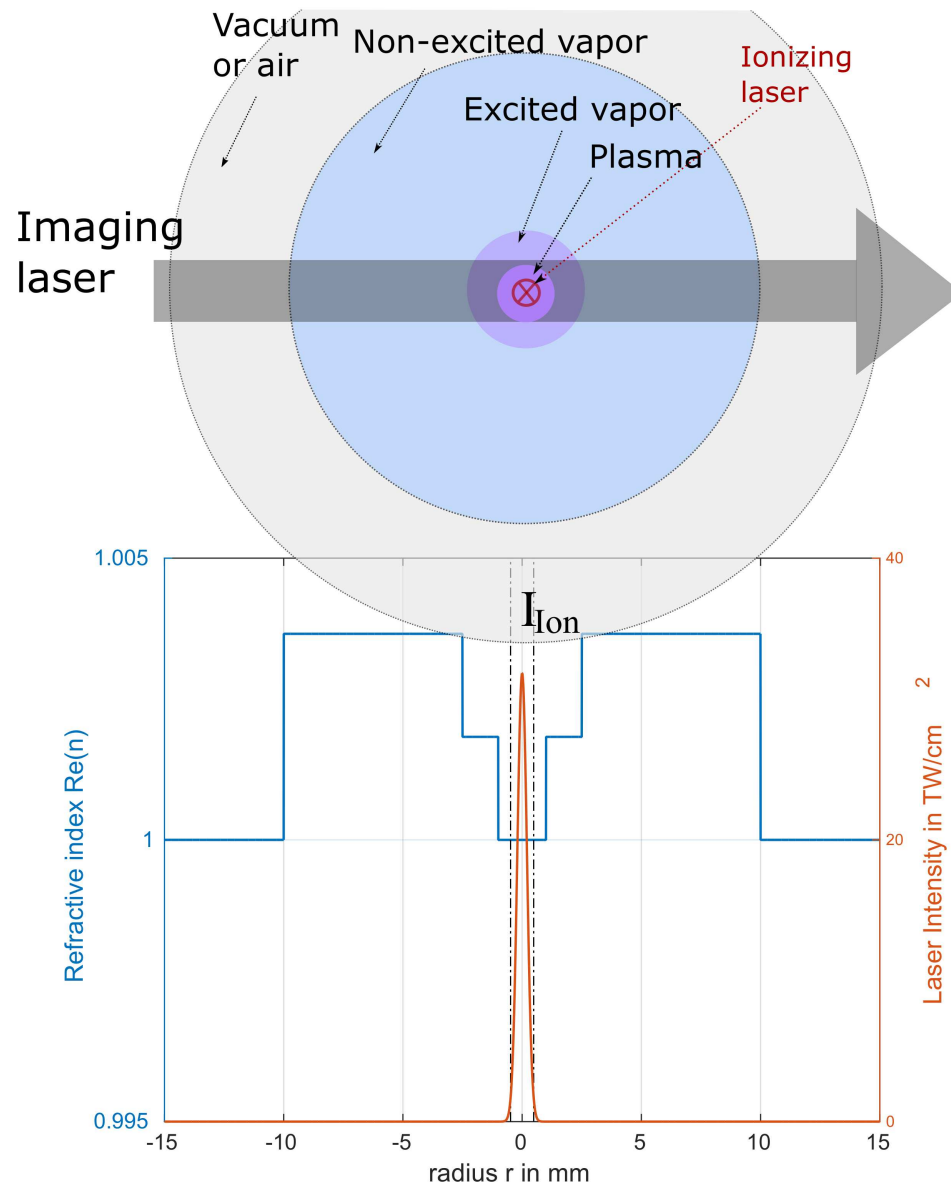


Figure 6.2: Refractive index of vacuum, non-excited and fully excited rubidium vapor and plasma for the AWAKE densities and a laser detuning frequency of $\Delta\nu = -5 \text{ GHz}$

6.2 Setup of the Experiment including Wavelength Determination using Spectroscopy

The following section describes the performance and the results of the experiment built at MPP. Sufficient excitation of rubidium atoms at the given density does not require a high-power laser, if the laser frequency can be tuned very close to an atomic transition with the ground state of the atom as the lower state. This lead to the decision to use the tunable CW-laser, originally only intended for the Schlieren imaging beam, also for the excitation of the rubidium atoms (pumping). This needs to be taken into account when analyzing the experimentally obtained radius of the excitation column using Schlieren imaging. For the experiments at CERN a suggested approach is to determine the imaging laser frequency leading to the strongest contrast of the plasma column image.

Here, by using the same laser beam for pumping and imaging, not only the phase shift caused by the object but also the object itself changes: The excitation column grows, shrinks or vanishes completely depending on the frequency and intensity of the pump laser.

6.2.1 Setup of the experiment at MPP

A sketch of the setup at MPP is depicted in Figure 6.3. It combines absorption spec-

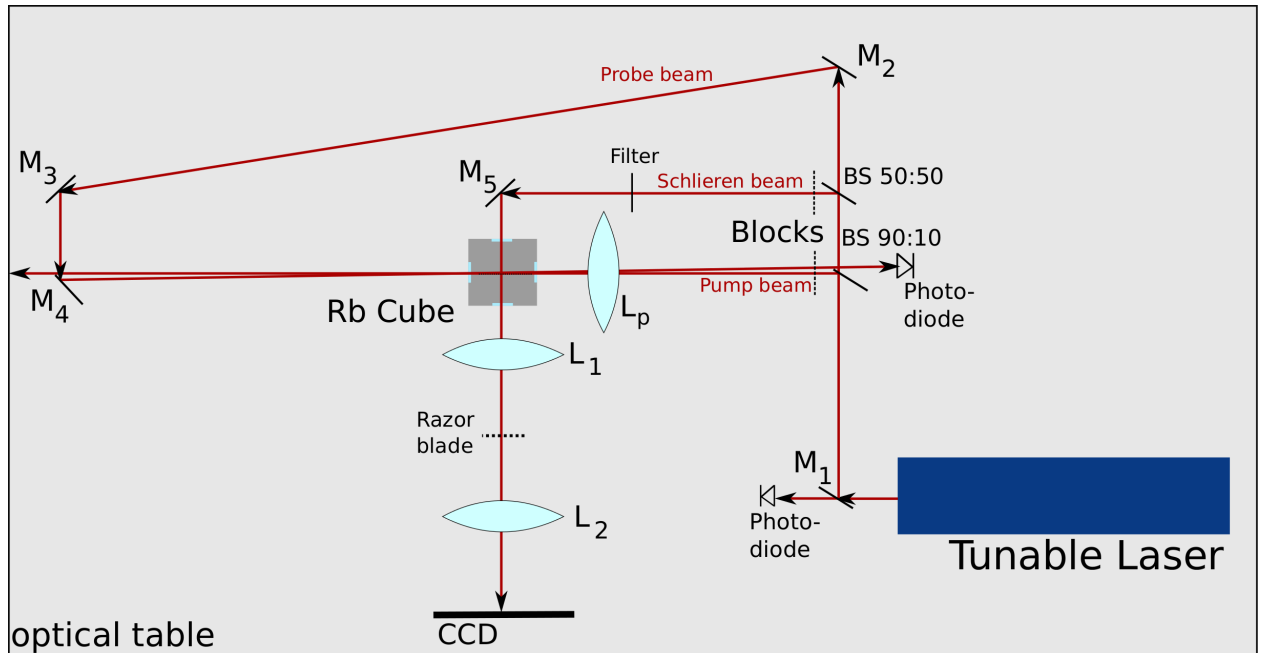


Figure 6.3: Setup at MPP for Schlieren Imaging of an Excited Vapor Column

troscopy for the frequency determination of the tunable laser with Schlieren imaging to measure the radius of the column of excited atoms and excitation of a Rb vapor column. The splitting of the laser beam leads to an additional challenge: While the pump beam should be fully absorbed for maximum pumping, the Schlieren beam should be fully transmitted. Since both beams originate from the same source they have the same frequency, a compromise has to be found.

Even if the laser is used solely as a Schlieren beam, as planned in the experiment at CERN, the set frequency requires a compromise: It needs to be close to the transition line to achieve a refractive index of the vapor different from 1 leading to the bending of the rays propagating through the column of excited or ionized atoms. At the same time it can not be arbitrarily close to the transition frequency of the D2 transition line, in which case the beam would be fully absorbed by the vapor.

The CCD camera used for the visualization of the gas jet will be used for recording the Schlieren images of the excitation column as well (Table 5.2). The lifetime of the atoms in the upper state $5P_{3/2}$ of the rubidium D2 transition line is 26 ns (Table 7.2). The thermal velocity of the atoms in 3D at $T = 250^\circ\text{C}$ is [12]

$$v = \sqrt{2 k_B T / m_{Rb}} \quad (6.1)$$

with $k_B = 1.38 \text{ J/K}$ the Boltzmann constant and $m_{Rb} = 1.4 \cdot 10^{-25} \text{ kg}$ the rubidium atom mass. It follows that on average atoms travel less than $7 \mu\text{m}$ within the lifetime of the excited state. Consequently, compared to the object size in the mm-range, the diffusion of the excited atoms due to thermal motion can be neglected in the following.

The specification of the tunable TOPTICA DLC DL pro laser is summarized in Table 6.2.

The sketch of the setup in Figure 6.3 shows three beams. The first one is reflected by

Wavelength	(763.1 – 813.6) nm
Line width	< 1 MHz
Maximal power	138 mW
Beam diameter	1 mm x 3 mm

Table 6.2: Data of the Tunable TOPTICA DLC DL pro laser

the beam splitter (90 : 10) guiding 90% of the intensity through the rubidium cell. This represents the pump beam, that is the beam creating the column of excited atoms to be visualized. A second beam splitter (50 : 50) divides the remaining 10% into the Schlieren beam to visualize the excited atom column and the probe beam for the wavelength determination using absorption spectroscopy. The intensity of the probe beam is measured

after propagating through the cell with a photo diode. The initial laser intensity during a frequency scan varies slightly. To compensate this effect the probe beam intensity on the photo diode is normalized using a second photo diode. It is placed at the exit of the laser, in this case behind the first mirror, marked as M_1 in Figure 6.3. The Schlieren beam needs to be attenuated before it enters the cell in order to prevent saturation through the vapor. After passing the rubidium cell it is propagating towards the CCD camera through the Schlieren setup consisting of the two lenses and the cutoff. In order to increase the size of the beam image on the CCD the first lens (" L_1 ") has a focal length of $f_1 = 150$ mm and the second lens (" L_2 ") of $f_2 = 200$ mm. This leads to a magnification of $4/3$. A razor blade is placed in the focal plane. In order to image the column of excitation generated by the pump beam properly, the spot size of the Schlieren beam needs to be larger than the column itself. While at CERN it is planned to increase the size of the Schlieren beam, in this experiment the size of the pump beam is decreased. It is focused onto the center of the cell through the lens " L_p " with the $f = 200$ mm lens. Schlieren imaging is very sensitive to any kind of disturbances. Uncoated optics, low quality view ports and scratches or dust can disturb the signal. For that reason a smaller sized pump beam was used. Since in the experiment at CERN the size of the ionizing laser is not supposed to be changed, a telescope is used to increase the size of the Schlieren beam before passing the cell.

All beams can be blocked independently.

6.2.2 Absorption Spectroscopy

Before heating up the rubidium cell, the laser frequency is determined by recording an absorption spectrum. The fine tuning of the laser frequency is controlled by applying voltage onto a piezo element, which as a result changes the cavity size of the laser. The frequency-voltage dependency is determined by absorption spectroscopy. Due to the arising absorption lines during a piezo voltage scan, the set piezo voltage can be assigned to the laser frequency. Meanwhile, the Schlieren beam is blocked to avoid an interaction with the vapor.

In Figure 6.5a the rubidium absorption spectrum around the transition line D2 is depicted. The scan covers and resolves the four lines of D2 line, originating from the 2 hyperfine ground states of each rubidium isotope ^{87}Rb and ^{85}Rb . Figure 6.4 illustrates the atomic structure of the two isotopes. In the scan the splitting of the ground states of the isotopes is resolved and is applied to the frequency determination. The piezo voltage can be converted to the laser frequency since the frequency differences between the lines are well known. The distances of the two lines are $\Delta\nu = 3.035$ GHz for ^{85}Rb and $\Delta\nu = 6.835$ GHz for ^{87}Rb . In the following piezo voltage to frequency conversion linearity of the laser is

assumed. This can be verified comparing the distances of two pairs of lines. The distance of the lines belonging to the ^{85}Rb isotope leads to the conversion $1\text{ V} \hat{=} 0.49\text{ GHz}$ and with the distance of the lines of ^{87}Rb it follows that $1\text{ V} \hat{=} 0.48\text{ GHz}$. In the following the distance between the two lines of the isotope ^{87}Rb is used. Figure 6.5b shows the scan after the conversion to the detuning frequency. The detuning frequency corresponds to the difference between the laser frequency and the center of the four lines of the D2 transition line.

In order to achieve a higher rubidium vapor density the reservoir and cell is heated up

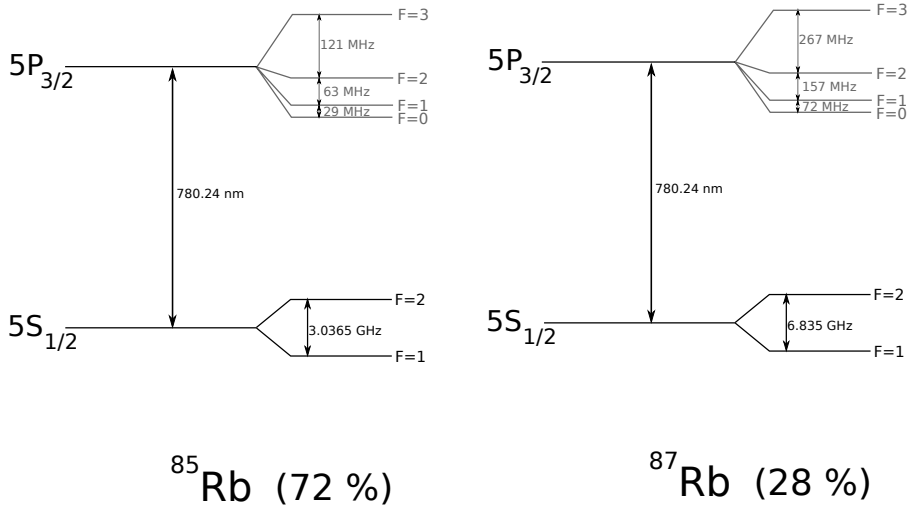


Figure 6.4: Atomic level structure of rubidium ^{87}Rb and ^{85}Rb [13]

subsequently. On the one hand, due to Doppler broadening and saturation the hyper fine structure of the D2 transition line is not resolved at high temperature ($T \geq 140^\circ\text{ C}$). The blue curve recorded at 40° C is compared with the red curve at 150° C in Figure 6.5. On the other hand, the high vapor temperature of more than 100° C is necessary for a signal of the excitation column using Schlieren imaging. Furthermore, this condition corresponds to the temperatures in the experiment of AWAKE. The higher the density the stronger the phase shift of the Schlieren beam and thus the stronger the signal of the excited atoms. However, there is an upper limit for the temperature because of the absorption of the Schlieren beam at higher densities, which should be avoided.

Due to the demand of different temperatures for spectroscopy and Schlieren imaging, the spectrum is recorded before heating up the cell to high temperatures of 150° C . Figure 6.6 shows the stability of the laser underlining that it is reasonable to determine the laser frequency before instead of during the measurement.

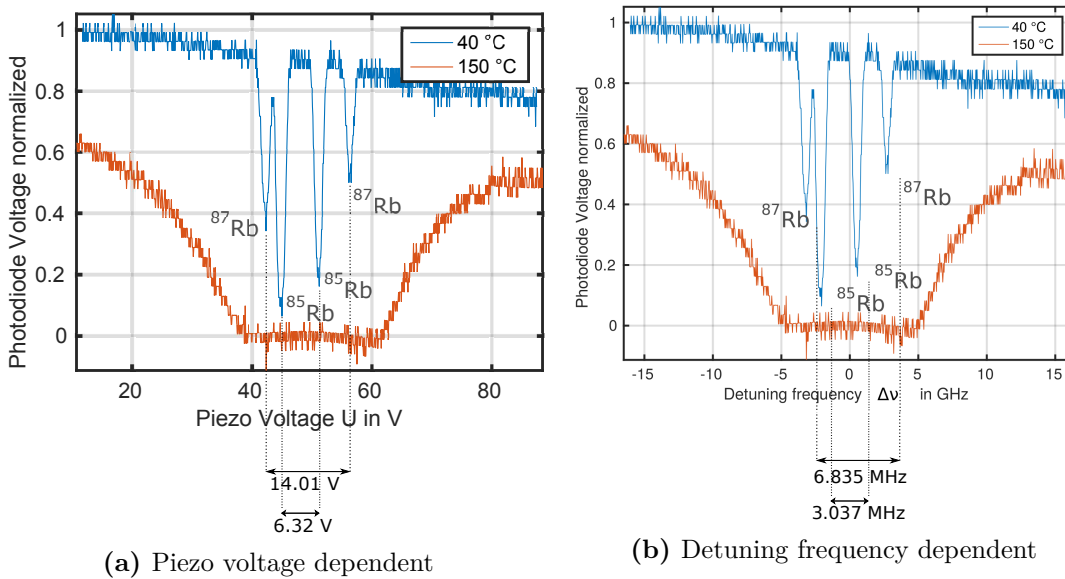


Figure 6.5: Absorption spectrum for laser frequency determination

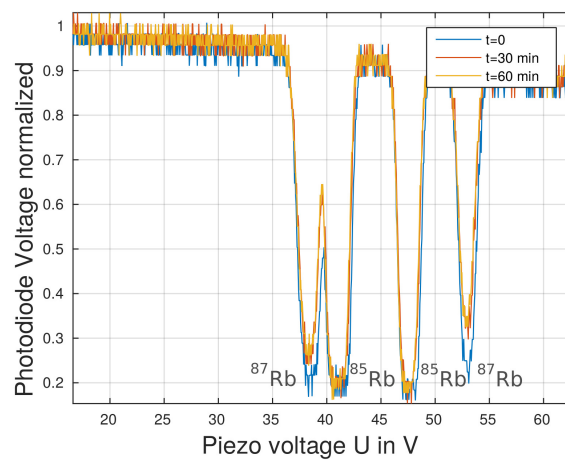


Figure 6.6: Stability of the laser over one hour

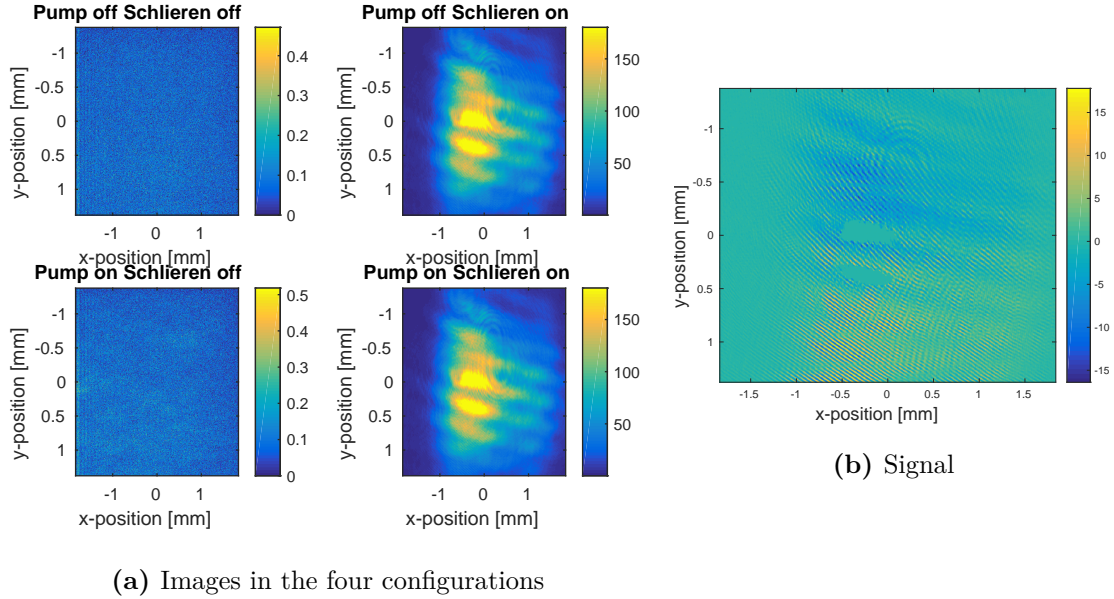
6.3 Frequency Dependent Schlieren Imaging Results

In the range of the frequency scan the excited atoms are visualized using Schlieren imaging. For this purpose, at each frequency four different configurations are set up, in which 15 images are recorded and averaged. During the measurement the probe beam of the spectroscopy is blocked before entering the cell. The two remaining beams are the pump and the Schlieren beam. The stated four configurations are the following:

1. "Pump off Schlieren off": In this configuration both beams are blocked, i.e. none of the beams propagate through the cell. An image recorded by the CCD corresponds to the noise of the camera. This is called "dark image". This image is subtracted from the images of all the other three configurations.
2. "Pump on Schlieren off": In this arrangement the Schlieren beam is blocked which means that only the pump beam propagates through the cell and excites atoms in the center. The light recorded by the CCD originates from reemitted photons. This can be helpful for focusing on the pump beam. Additionally it can be checked whether the two beams overlap properly. This image needs to be subtracted from the signal of the Schlieren image as well, since it is not the aim to visualize reemitted photons but only the phase shift of the Schlieren beam.
3. "Pump off Schlieren on": In this case the pump beam is blocked, i.e. there are no excited atoms in the center acting as the transparent object. By subtracting this image from the final image the contrast of the signal can be increased.
4. "Pump on Schlieren on": Without any beam dump both beams, the Schlieren and the pump beam, propagate through the cell. The images of the two previous configurations must be subtracted from this image to receive the final image of the object, which is called the "signal" in the following.

6.3.1 Schlieren Imaging at a Low Temperature

Figure 6.7 demonstrates the result of Schlieren imaging at a low rubidium temperature ($T = 50^{\circ}\text{C}$). Figure 6.7a presents the average of the images taken in the four configuration explained above. The top left image, the noise of the CCD, has already been subtracted from the other three images. To uncover the information of the excited atoms the processing explained above is applied to the images. This results in the signal depicted in Figure 6.7b. A light distribution with weak intensity values, but a lower intensity at the top and a higher at the bottom, arises. Nevertheless, the phase shift and therefore the sig-



(a) Images in the four configurations

Figure 6.7: Images at low temperature ($T = 50^\circ\text{C}$) at $\Delta\nu = -1.2 \text{ GHz}$

nal can be enhanced by operating at higher temperatures. In the following measurements the cell is heated up to $T = 150^\circ\text{C}$.

6.3.2 Schlieren Imaging without a Cutoff

In chapter 3 it is explained why the cutoff in the focal plane is necessary using Schlieren imaging. This is demonstrated in Figure 6.8 and Figure 6.9. Once more, images in the four configurations are recorded, as depicted on the left hand side, and the processing leads to the signal on the right hand side. Without a cutoff the column of excited atoms is not visible, see Figure 6.8b. With a razor blade as a knife edge, blocking the undeflected and the downwards deflected rays the object becomes clearly visible, as seen in Figure 6.9b. The Schlieren beam is defocused by the excited Rb column, i.e. the rays from the lower half of the column are bent downwards and blocked by the knife edge. This leads to a lack of light on the camera at the lower half of the column. Rays from the upper half of the excited Rb column are bent upwards, can pass the knife edge and lead to a higher intensity on the CCD camera. As a remark, the image is inverted by lens L_2 in Figure 6.3 but flipped once more by the camera.

The following results were obtained using a horizontal razor blade as cutoff.

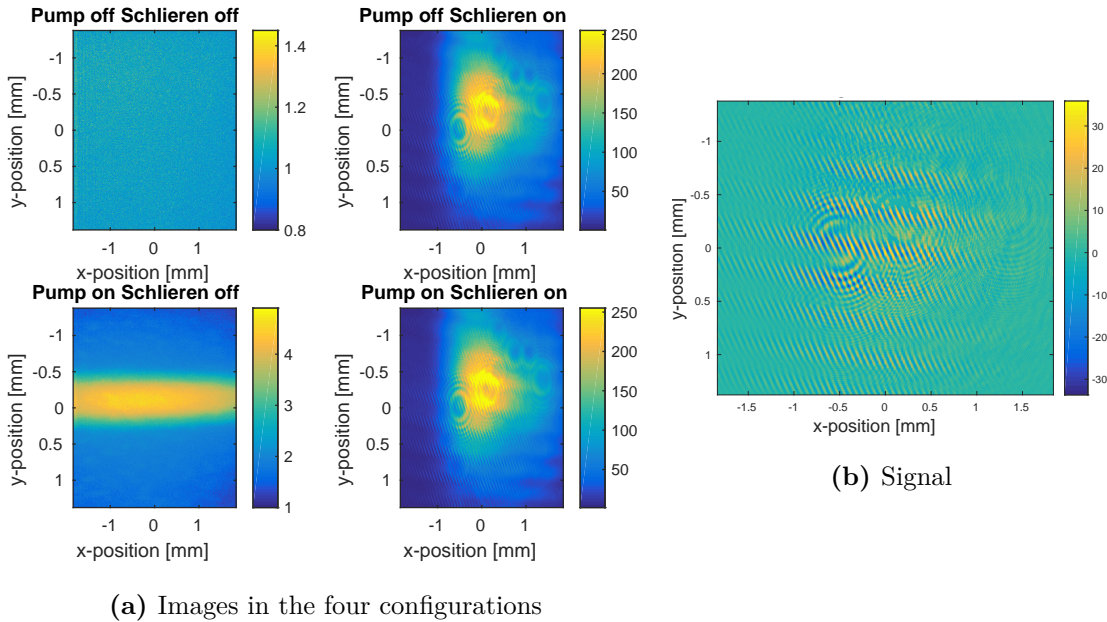


Figure 6.8: Recorder images without cutoff at high temperature ($T = 150^\circ\text{C}$) at $\Delta\nu = -8.7 \text{ GHz}$

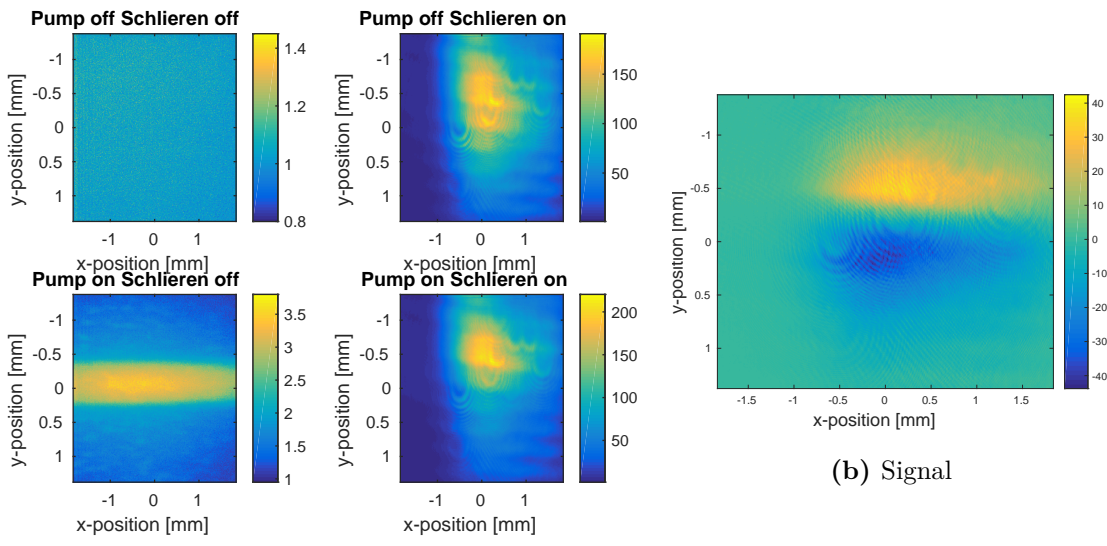


Figure 6.9: Recorder images with knife edge cutoff at high temperature ($T = 150^\circ\text{C}$) at $\Delta\nu = -8.7 \text{ GHz}$

6.3.3 Schlieren Imaging at High Temperatures

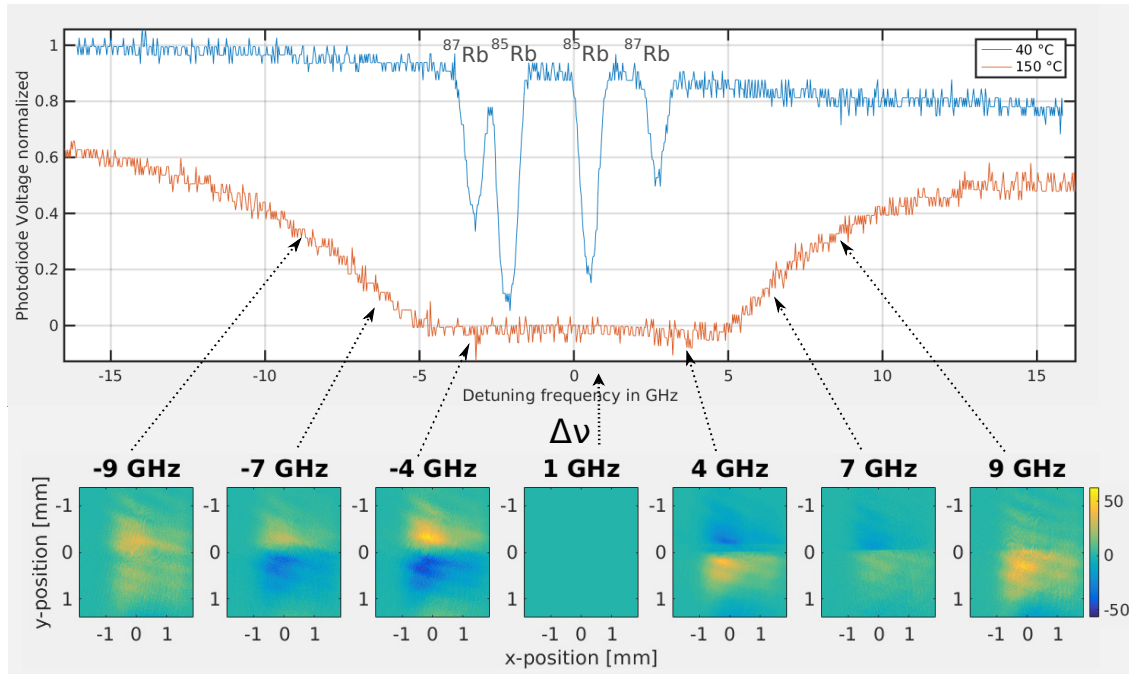


Figure 6.10: Recorder images with a knife edge at high temperature ($T = 150^\circ\text{C}$) at different detuning frequencies $\Delta\nu$

Figure 6.10 shows the comparison of the signal of the excitation column for different laser frequencies. During the measurement in this section the razor blade stays put. The aim is to find the laser frequency for the strongest signal. For detuning frequencies $\Delta\nu \gtrsim \pm 9 \text{ GHz}$ the signal starts to smear out. Either the pump does not sufficiently excite (due to the difference between the laser and the transition frequency) or the phase shift in the Schlieren beam was not strong enough, because the refractive index of the non-excited vapor converges to 1. Approaching the transition frequency the signal becomes stronger, since on the one hand the excitation by the pump beam increases and on the other hand the difference in the refractive indices between non-excited and excited vapor increases. Unfortunately the laser frequency can not be approached to the transition frequency arbitrarily: If the laser frequency is too close to the transition frequency the Schlieren beam is absorbed and the image recorded by the CCD vanishes, as depicted in the central image of Figure 6.10 obtained with a detuning frequency $\Delta\nu = 1 \text{ GHz}$.

Figure 6.10 clearly illustrates the change in the refractive index of the vapor at the transition frequency (as seen in Figure 6.1). As explained before, on one side of the transition line, in case of negative detuning frequency, the refractive index is larger than 1. On the

other side, for a positive detuning frequency, it is smaller than one. This implies that the sign of the difference between the non-excited vapor ($\hat{=}$ surrounding medium) and the excited vapor ($\hat{=}$ object) changes. For a detuning frequency $\Delta\nu < 0$ the refractive index of excited vapor is smaller than that of non-excited vapor ($n_{\text{excited vapor}} < n_{\text{non-excited vapor}}$), i.e. the Schlieren beam is defocused. Therefore, the rays bent from the lower part of the excited Rb column are blocked and the lower part of the column appears dark in the image of the CCD. For a detuning frequency $\Delta\nu > 0$ the refractive index of excited vapor is larger than that of non-excited vapor ($n_{\text{excited vapor}} > n_{\text{non-excited vapor}}$), i.e. the Schlieren beam is focused. In this case, rays bent from the upper part of the excited Rb column are blocked which leads the upper part of the column appear dark in the image of the CCD.

6.3.4 Radius Determination of the Excited Channel

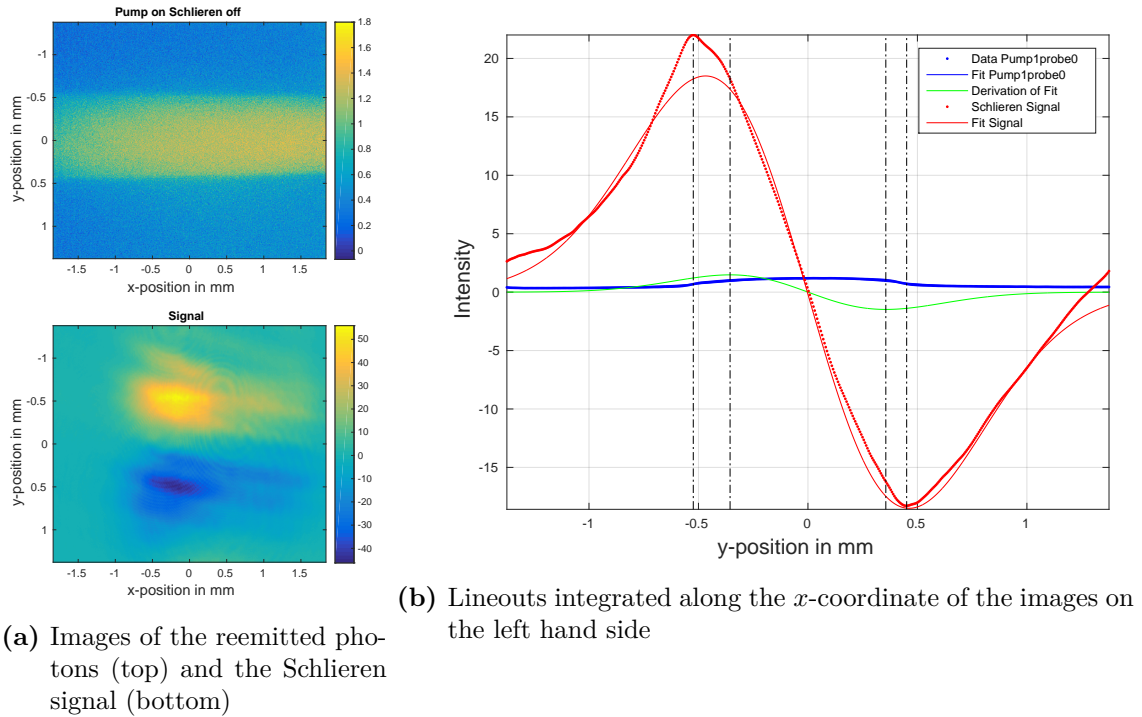


Figure 6.11: Recorder images with cutoff at high temperature ($T = 150^\circ\text{C}$) at $\Delta\nu = -1.9 \text{ GHz}$

As explained in section 3.3, the signal obtained through Schlieren imaging responds to the first derivative, i.e. the change of the refractive index. Due to the Gaussian beam profile a similar distribution of excited atoms is expected. This consideration is analyzed

in Figure 6.11a.

The top left image in Figure 6.11 shows the reemitted photons from the atoms, excited by the pump beam, while the Schlieren beam is blocked. The bottom left one corresponds to the Schlieren signal after the imaging processing. The aim is to determine the radius of the excitation column. For this purpose the intensity is averaged along the x -coordinate in the two images. The resulting lineouts along y are given on the right hand side. The blue dots correspond to the top and the red dots correspond to the bottom image. It can be seen that the intensity of the Schlieren signal is significantly higher than the signal obtained by recording the reemitted photons. The intensity of the top image is approximately constant along x , while the signal at the bottom originates from the Schlieren beam, recorded head on. Averaging the bottom image over x decreases the signal due to the lack of light at the edges of the sensor. Consequently the signal appears to show lower intensities in the lineout.

Both data curves are fitted. The light from the pump beam is fitted with a Gaussian function (blue solid curve). The signal obtained using Schlieren imaging is expected to respond to the derivative of the refractive index. In the case of a constant refractive index of the object, this corresponds to the derivative of the object shape. That is why the red data points are fitted using the derivative of a Gaussian function, resulting in two Gaussian functions (red solid curve). To demonstrate the theoretical considerations the derivative of the (blue) Gaussian fit is plotted as a green curve. The course of the graph is compared with the recorded Schlieren signal (red dots). The dashed black vertical lines indicate the extrema of the green curve and of the red data points of the Schlieren signal. Integration of the two Gaussian curves it should allow the determination of the Gaussian shape of the object and with this its size. The similar extrema positions of the two curves support the assumption that the object can be reconstructed.

Figure 6.12 presents the position of the extrema for measurements using different laser frequencies. A similar trend in the minimum and maximum can be observed: Approaching the transition frequency with a negative detuning frequency the object size derived from the recording of the reemitted photons as well as from the signal of Schlieren imaging increases. This is in agreement with the theory: Approaching the transition frequency with a lower frequency the pump beam broadens in the rubidium vapor. The size determined from the Schlieren signal is always larger than the size obtained by the reemission. This could be due to the very low signal of the reemitted photons, i.e. photons emitted from atoms with a larger radius could not be detected due to the low intensity.

According to the results obtained with Schlieren imaging the diameter of the excitation column increases with a detuning frequency from $\Delta\nu = -16 \text{ GHz}$ to $\Delta\nu = -1.9 \text{ GHz}$ from $d_{-16 \text{ GHz}} = 0.35 \text{ mm}$ to $d_{-1.9 \text{ GHz}} = 0.97 \text{ mm}$. For comparison in the image of the reemitted

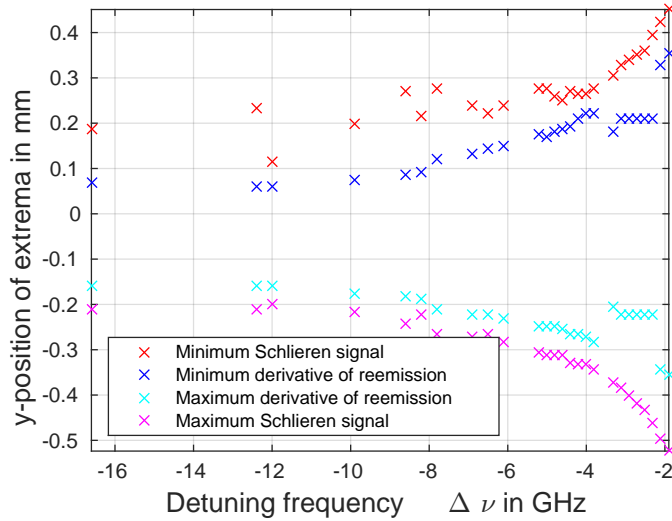


Figure 6.12: Extrema position of the intensity line outs

photons the size increases from $d_{-16\text{ GHz}} = 0.28\text{ mm}$ to $d_{-1.9\text{ GHz}} = 0.71\text{ mm}$. Respecting the magnification of the two lenses of the Schlieren setup this corresponds to a radius of $0.13\text{ mm} < r < 0.36\text{ mm}$ for the Schlieren signal and $0.11\text{ mm} < r < 0.27\text{ mm}$ for the image of reemitted photons. As already mentioned, the pump beam was focused onto the center of the rubidium cell meaning that the actual size of the beam is not known at this point. As explained before, the Schlieren signal of the excitation column increases approaching the transition line due to the stronger excitation and the larger difference of the refractive indices. The intensity increase of the extrema of the lineouts upon approaching the transition line is plotted in Figure 6.13.

In order to study Schlieren imaging technique, it is disadvantageous to use the same laser as a pump and a Schlieren beam since the visualized object changes. Especially on the right side of the transition frequency, i.e. when approaching the transition frequency with a higher laser frequency, different unintended effects like filament propagation occur. Here neither the reemitted photons appear as a Gaussian distribution, nor the lineout of the signal obtained from Schlieren imaging corresponds to the derivative of a Gaussian function. Therefore the consideration of the object as a column with a certain radius is not valid any more. This is illustrated in the line out in Figure 6.14.

Further studies are necessary at this point. The pump beam head on after the cell is studied in a separate measurement in subsection 6.3.5.

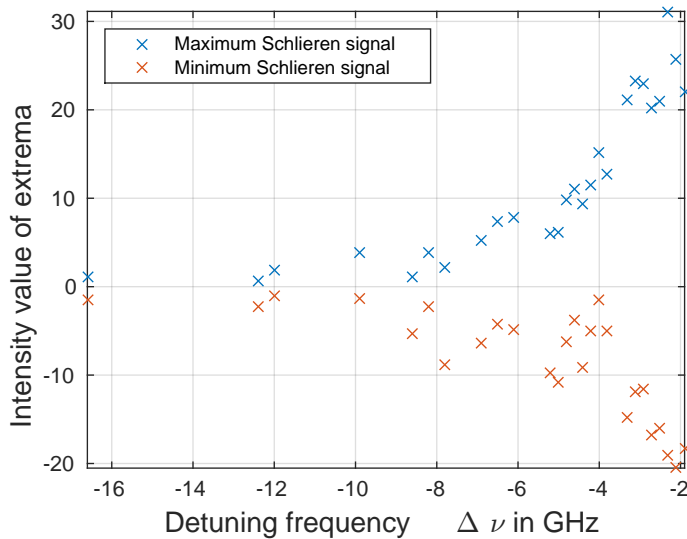


Figure 6.13: Intensity value of the extrema of the intensity line outs

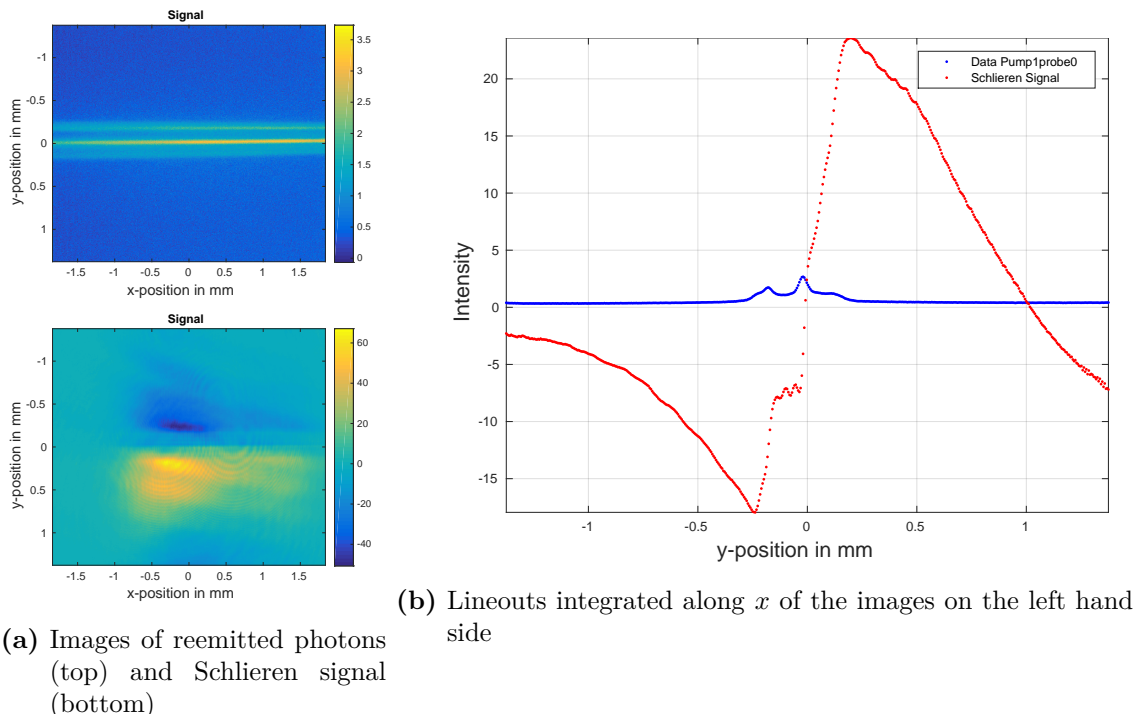


Figure 6.14: Records with a cutoff at high temperature ($T = 150^\circ C$) at $\Delta\nu = 4.4$ GHz

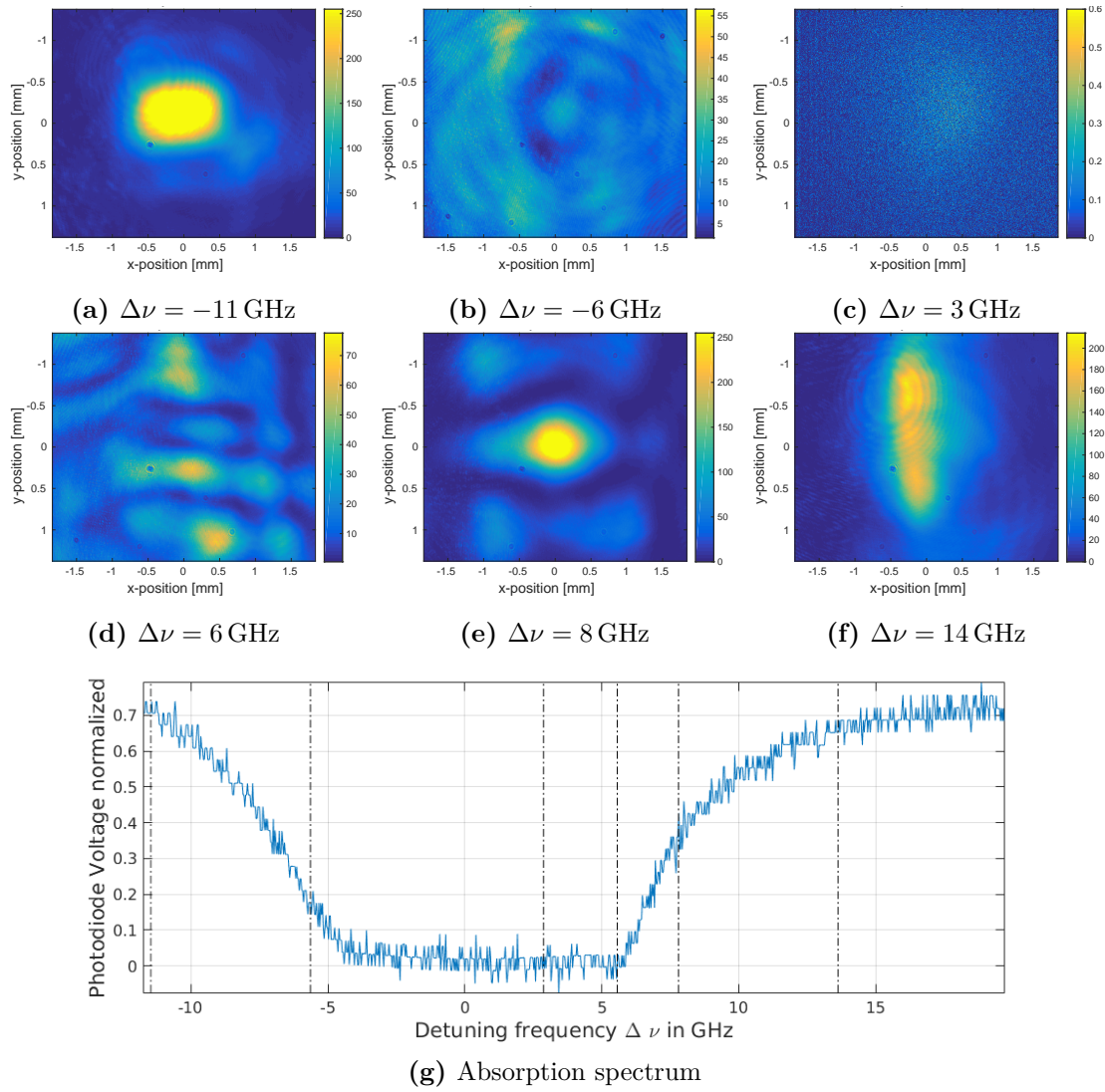


Figure 6.15: Head on pump beam at high temperature ($T = 150^\circ\text{C}$)

6.3.5 Study of the Pump Beam close to the Transition Frequency

Figure 6.15 shows images of the pump beam recorded with the CCD camera head on after propagation through the cell. The images correspond to a different run, thus the frequency can not be compared directly with Figure 6.10. Though they demonstrate the effects on the pump beam at frequencies very close to the transition line. In the experiment at CERN an ionizing laser with a broad spectrum is used for pumping. The experiment at MPP uses the tunable laser for pumping, too. This laser has a narrow linewidth, which leads to strong absorption and non-linear effects close to the transition line. If the laser frequency approaches the transition frequency from lower frequencies the initial Gaussian beam (Figure 6.15a) broadens, as seen in Figure 6.15b. Once the frequency is too close to the transition frequency, the beam is absorbed completely, as recorded in Figure 6.15c. In case of slightly higher frequencies the beam is focused. Filament propagation is observed on this side of the transition line, as can be seen in Figure 6.15d.

For frequencies below the transition frequency, the refractive index of vapor is larger than

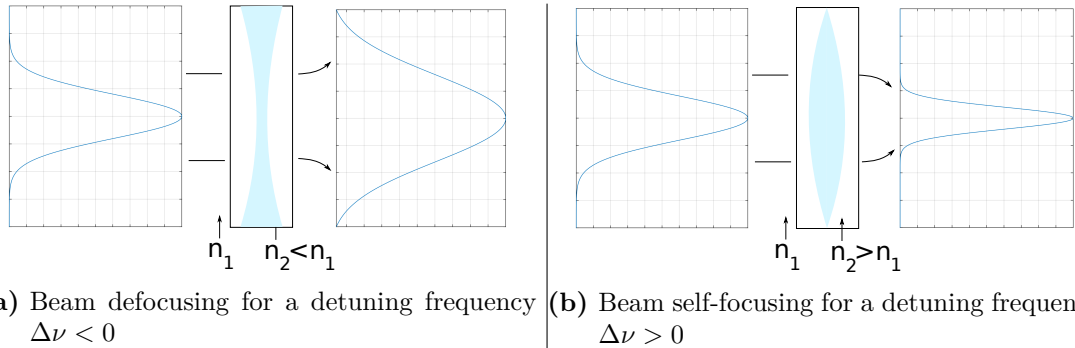


Figure 6.16: De- and focusing effect of the beam propagating through a medium with changing refractive index [14]

one $n_{non-excited} = 1 + dn$. Since in a 2 level atom system maximal excitation corresponds to $N_1 = N_t/2$, the refractive index of the excited vapor is between $1 + \frac{dn}{2} < n_{excited} < 1 + dn$, i.e. the beam propagates through a medium with smaller refractive index. Similarly, for frequencies above the transition frequency the refractive index of excited vapor is between $1 - dn < n_{excited} < 1 - \frac{dn}{2}$, i.e. the beam propagates through a medium with a higher refractive index.

Since the pump beam follows a Gaussian intensity distribution, the intensity is higher in the center, which also leads to stronger excitation. Therefore, for a detuning frequency $\Delta\nu > 0$ the refractive index is higher in the center compared to the wings. This leads to a focusing power, comparable to a lens, as sketched in Figure 6.16b. The focusing itself then reinforces this effect due to the increasing intensity in the center. This is called "self-

focusing” [14]. The same considerations can be made for a negative detuning frequency: the higher intensity at the center leads to a higher number of excited atoms and consequently to a stronger decreasing refractive index in the center as in the wings. This effect induces a defocusing of the beam while propagating, as seen in Figure 6.16a. In contrast to the self-focusing this effect does not reinforce itself.

In the experiment at CERN this is not expected to be an issue, since the laser is broadband and only a very small part of the spectrum is at a frequency very close to the transition frequency.

7 Outlook: Plasma Radius Measurement at CERN

The radius measurement of the excitation column should be applied to the plasma column in the experiment at CERN. Figure 7.1 shows the planned setup at CERN. It is similar

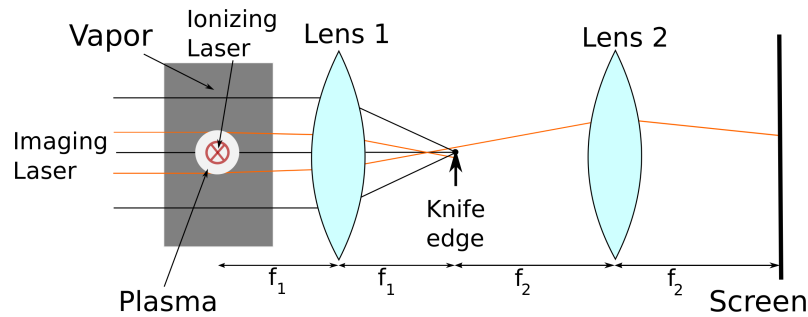


Figure 7.1: Setup for Schlieren imaging at CERN

Power P	4 TW
Duration $\Delta\tau$	100 fs
Wavelength λ	(780 \pm 10) nm

Table 7.1: Specification ionizing laser at CERN

to the setup built at MPP. In this experiment a high intensity pulsed laser is used as the pump laser for the excitation and ionization of the rubidium vapor in the 10 m-long cell. The properties of the laser are summarized in Table 7.1. The ionization intensity of rubidium is $I_{Ion} \approx 1.7 \cdot 10^{12} \text{ Wcm}^{-2}$. For the utilized laser the intensity is expected to be larger than the ionization intensity for a radius of up to $r \leq 1 \text{ mm}$ over a propagation distance of $z = 10 \text{ m}$. Due to the wavelength spectrum and the intensity it is expected that excitation and ionization will occur in the vapor cell.

The experiment presented in chapter 6 showed that a column of excited atoms can be visualized using Schlieren imaging for the rubidium densities examined in the AWAKE project. For this purpose a CW-laser was used for pumping and imaging. Due to that the integration time of the image was determined by the integration time of the CCD

(Table 5.2) with $58 \mu\text{s}$ as a lower limit.

At CERN the pumping laser is a pulsed laser, i.e. according to the respective lifetime the existence of excited and ionized atoms is very short. Due to the broadband laser, the rubidium atoms will be excited to different energy levels. The energy levels of rubidium and their corresponding allowed transitions are depicted in Figure 7.2. The laser will be resonant with the previously discussed 780 nm D2-line but also with the 795 nm D1-line of rubidium. In addition shorter wavelengths of the laser spectrum (more precisely 762 nm and 776 nm) will raise excited atoms ($5^2P_{1/2}$ and $5^2P_{3/2}$) to even higher energy levels ($5^2D_{3/2}$ and $5^2D_{5/2}$). This effect increases the ionization rate at AWAKE, since from the $5^2D_{5/2}$ -state the ionization potential is much lower than from the ground state.

The related lifetimes of the excited states of rubidium are listed in Table 7.2 . Compared

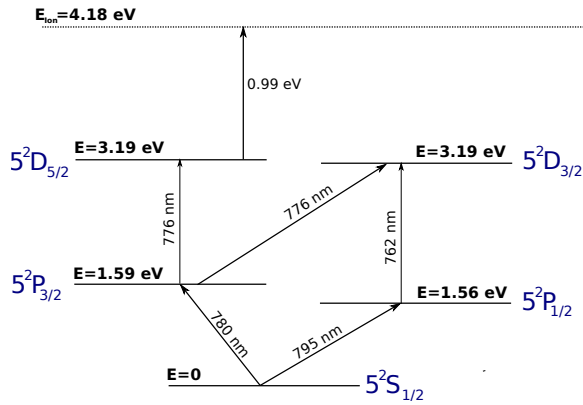


Figure 7.2: Energy levels of Rubidium ^{85}Rb and ^{87}Rb [15]

State	Lifetime τ in ns
$5^2D_{3/2}$	230
$5^2D_{5/2}$	230
$5^2P_{3/2}$	26
$5^2P_{1/2}$	28

Table 7.2: Lifetimes of the excited states of rubidium [16],[13]

to the lifetimes of the excited states, the lifetime of the plasma created in the framework of AWAKE (with a plasma density of $n_{pe} \approx 10^{15} \text{ cm}^{-3}$) is expected to be in the μs -scale [5].

The timescales are much lower than the integration time of the CCD. If a CW laser is used for imaging, the signal of the excited or ionized matter will be very small if light is collected over the relatively long integration time. Either the imaging laser must be pulsed or the CCD has to be very fast to yield a strong signal of the transparent object. This

leads to the decision to use a gated camera in the experiment at CERN. Whether enough light originating from the tunable laser during the short integration time can be collected, is tested by using the gated camera for the visualization of the excitation column in the setup at MPP.

The gated camera is an ANDOR "iStar 334T" intensified CCD. Images were recorded with the settings summarized in Table 7.3. Since a CCD gain of 2000 is set, the width of the gain, not the exposure time, is crucial and defines the integration time of the light.

The images in Figure 7.3, recorded with a detuning of $\Delta\nu = -3.9$ GHz, demonstrate that

Gain	2000
Gain Width	10 ns
Exposure Time	10 μ s

Table 7.3: Settings of the gated camera from ANDOR

even at a timescale of 10 ns, which is below the shortest lifetime of the energy levels of rubidium, only a weak signal of the excitation column is visible. The images at the top are taken with the Manta CCD without gain but with an exposure time of 58 μ s. These images serve as a comparison. The column which appears bright at the top and dark at the bottom also becomes visible in case of the short integration time of the gated camera. These results indicate that the combination of the tunable CW-laser from TOPTICA with the ANDOR gated camera is suitable for the measurements at CERN.

Further studies are necessary to find out, whether not only the appearance of excited vapor but also the disappearance of the excited vapor due to the ionization can be observed. This is required to determine the radius of the plasma channel in the rubidium cell in the AWAKE project.

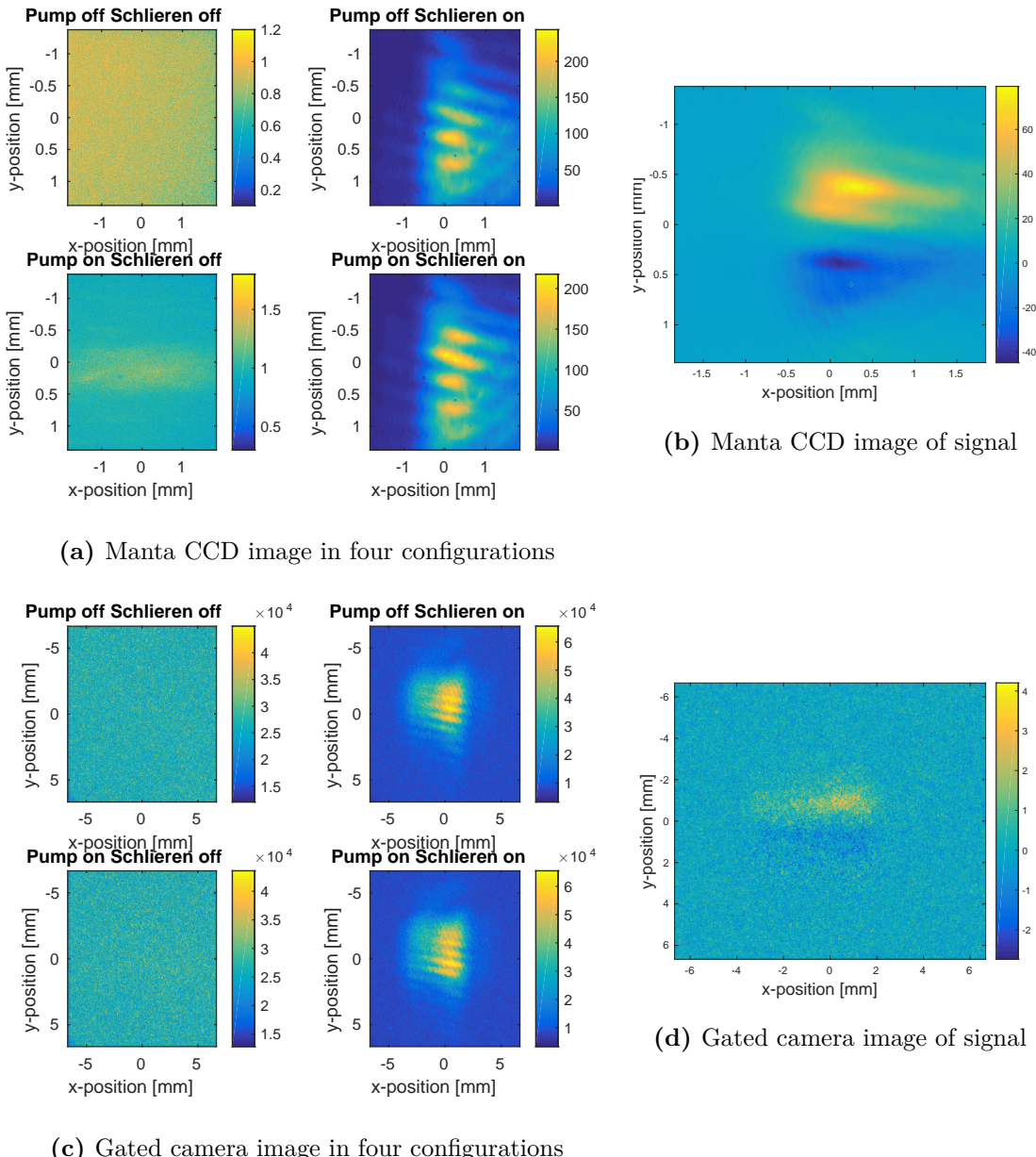


Figure 7.3: Comparison of the results of Schlieren imaging with the Manta CCD and a gated camera for a detuning of $\Delta\nu = -3.9$ GHz

8 Conclusion

In the framework of AWAKE a new plasma wakefield accelerator with a proton bunch as a driver is developed. The bunch propagates through a 10 m long rubidium plasma, induced by an ionizing laser pulse. For the purposes of AWAKE and for the efficient acceleration of particles, for instance electrons, the plasma column must have a radius larger than 1 mm. In the present thesis, Schlieren imaging is investigated as a method to measure plasma radius.

Schlieren imaging enables the visualization of transparent objects with a different refractive index than the surrounding medium visible. The light is bent by the object and can pass a block, absorbing non-deflected rays. This increases the contrast.

First, density perturbations in ambient air were imaged by this technique. The size and shape of the perturbations were clearly recognizable.

Then a column of excited atoms was visualized using Schlieren imaging. In this case a tunable laser with a wavelength very close to the transition wavelength of the D2 line of rubidium was used. This leads to a refractive index significantly different from 1. The excitation column lead to a strong Schlieren signal. From the measurement the radius of the channel was determined.

This discovery should be applied to the case of ionization in the experiment at CERN. The difference of the refractive index of plasma and fully excited vapor is the same as fully excited vapor and vapor in the ground state. This is why it is expected that one can apply the developed method to the plasma radius measurement. Calculations using physical optics also showed that Schlieren imaging is sufficient for this purpose considering the refractive index of plasma and the expected size of the channel.

The remaining question to be answered is, whether a distinction between the excited vapor and the plasma can be made experimentally. An alternative approach is to make use of the fact that the lifetime of the excited states is short compared to the lifetime of the plasma. Measuring the channel radius with some delay to the ionizing laser pulse, you obtain an image of the plasma column inside of the vapor in the ground state without surrounding excited atoms.

List of Figures

1.1	Principle of AWAKE	5
1.2	Sketch of the Rubidium Cell with Plasma Radius Diagnostic	6
2.1	Wakefield in Linear Wakefield Theory along ζ	10
2.2	Transverse Wakefield in Linear Wakefield Theory	11
2.3	Seeding of Self Modulation Instability	13
2.4	Beam and Plasma Density Structure with SMI	14
3.1	Change of the Wave Phase Planes caused by an Object	16
3.2	Sketch of Direct Shadowgraphy	17
3.3	Sketch of Direct Shadowgraphy with Converging Lens	18
3.4	Sketch of a Simple Schlieren System	18
3.5	Appearance of a Cylindrical Symmetric Object on the Screen using Schlieren Imaging with a Knife Edge	20
3.6	Schlieren Images of a Gas Jet with Different Cutoffs	21
4.1	Sketch of the Setup in the Calculations	25
4.2	Initial Gaussian Beam and Phase Shift in the Calculations	27
4.3	Calculated Images in the Absence of an Object or a Cutoff	28
4.4	Calculated Schlieren Image of a Plasma Column	28
5.1	Sketch of the Setup for Schlieren Imaging of Density Perturbations	29
5.2	Density Perturbation through a Gas Jet using Schlieren Imaging	31
6.1	Index of Refraction of the Rubidium Vapor near the D2 Transition Line . .	33
6.2	Comparison of the Index of Refraction of Vacuum or Air, Non-excited and Fully Excited Rubidium Vapor	35
6.3	Setup at MPP for Schlieren Imaging of an Excitation Column	36
6.4	Atomic Level Structure of Rubidium	39
6.5	Rubidium Absorption Spectrum for Laser Frequency Determination	40
6.6	Laser Stability Test	40

6.7	Schlieren Image at Low Rubidium Temperature	42
6.8	Schlieren Image at High Rubidium Temperature without Cutoff	43
6.9	Schlieren Image at High Rubidium Temperature with Knife Edge as Cutoff	43
6.10	Schlieren Images for Different Laser Frequencies	44
6.11	Radius Determination of the Excitation Column with Schlieren Imaging . .	45
6.12	Intensity Extrema Positions of the Schlieren Images	47
6.13	Intensities of Schlieren Signal	48
6.14	Schlieren Image with a Positive Detuning Frequency	48
6.15	Pump Beam Effects around the Transition Line	49
6.16	Focusing and Defocusing of a Laser Beam in a Medium	50
7.1	Schlieren Imaging Setup at CERN	52
7.2	Energy Levels of Rubidium	53
7.3	Comparison of Schlieren Images recorded with the Manta CCD camera and the Gated Camera	55

Bibliography

- [1] K. V. Lotov, A. P. Sosedkin, A. V. Petrenko, et al. Electron trapping and acceleration by the plasma wakefield of a self-modulating proton beam. *Phys. Plasmas 21, 123116*, 2014.
- [2] Brent Edward Blue. Hosing Instability of the Drive Electron Beam in the E157 Plasma-Wakefield Acceleration Experiment at the Stanford Linear Accelerator. 2000. <http://www.slac.stanford.edu/cgi-wrap/getdoc/slac-r-783.pdf>.
- [3] S.V. Kuzikov, M.E. Plotkin, et al. Concepts for rasing rf breakdown threshold by using multi-moded cavities. 2010.
- [4] P. Muggli, A. Caldwell, O. Reimann, et al. Physics of the Awake Project. *Proceedings of IPAC, TUPEA008*, 2013.
- [5] Francis F. Chen. *Introduction to Plasma Physics*. Plenum Press, New York, 1974.
- [6] Yun Fang. Resonant Excitation of Plasma Wakefield. 2014. <http://digitallibrary.usc.edu/cdm/ref/collection/p15799coll3/id/362522>.
- [7] R. Assmann, R Bingham, et al. Proton-driven plasma wakefield acceleration: a path to the future of high-energy particle physics. *IOP Publishing Ltd*, 2014.
- [8] Naveen Kumar, Alexander Pukhov, and Konstantin Lotov. Self-Modulation Instability of a Long Proton Bunch in Plasmas. *Physical Review Letters 104, 255003*, 2010.
- [9] G. S. Settles. *Schlieren and Shadowgraph Techniques*. Springer, 2001.
- [10] W. Demtröder. *Laserspektroskopie*. Springer, 2007.
- [11] O. Svelto. *Principles of Lasers*. Springer, 1998.
- [12] W. Demtröder. *Experimentalphysik 3 Atome, Moleküle und Festkörper*. Springer, 2010.
- [13] Daniel A. Steck. Rubidium 87 D Line Data. 2008. <http://steck.us/alkalidata>.

- [14] A. E. Siegman. *Lasers*. University Science Books, 1986.
- [15] J. E. Sansonetti. Wavelengths, Transition Probabilities, and Energy Levels for the Spectra of Rubidium (RbI through RbXXXVII). *Phys. Chem. Ref. Data, Vol. 35, No. 1.*, 2006.
- [16] J Marek and P Munster. Radiative lifetimes of excited states of rubidium up to quantum number n=12. *J. Phys. B: At. Mol. Phy. 14* 201, 1981.

Acknowledgment

Affidavit

”I hereby declare

1. that I completed the Term Paper without external help
2. that I indicated the use of literal citations from literature as well as the use of the ideas of other authors at their respective places in the paper.

I am aware of the fact that an untrue declaration will have legal consequences.”

Munich, the 21th of December 2016

Anna-Maria Bachmann